Distribution Categories:
Magnetic Fusion Energy (UC-20)
--Plasma Systems (UC-20a)
--Magnetic Systems (UC-20b)
--Reactor Materials (UC-20c)
--Fusion Systems (UC-20d)

ANL/FPP/TM-185

ANL/FPP/TM--185

DE84 014839

ARGONNE NATIONAL LABORATORY
9700 South Cass Avenue
Argonne, Illinois 60439

A COMPARATIVE STUDY OF PULSED AND STEADY-STATE TOKAMAK REACTOR BURN CYCLES

by

D. A. Ehst, J. N. Brooks, Y. Cha, K. Evans,
A. M. Hassanein, S. Kim, S. Majumdar,
B. Misra, and H. C. Stevens

Fusion Power Program

May 1984

TABLE OF CONTENTS

LIST OF FIGURES

A COMPARATIVE STUDY OF PULSED AND STEADY-STATE TOKAMAK REACTOR BURN CYCLES

D. A. Ehst, J. N. Brooks, Y. Cha, K. Evans, Jr.,
A. M. Hassanein, S. Kim, S. Majumdar,
B. Misra, and H. C. Stevens

Fusion Power Program

ABSTRACT

Four distinct operating modes have been proposed for tokamaks. Our study focuses on capital costs and lifetime limitations of reactor subsystems in an attempt to quantify sensitivity to pulsed operation. Major problem areas considered include: thermal fatigue on first wall, limiter/divertor; thermal energy storage; fatigue in pulsed poloidal field coils; out-of-plane fatigue and eddy current heating in toroidal field coils; electric power supply costs; and noninductive driver costs. We assume a high availability and low cost of energy will be mandatory for a commercial fusion reactor, and we characterize improvements in physics and engineering which will help achieve these goals for different burn cycles.

1. INTRODUCTION

The tokamak was originally envisioned to provide the basis for a fusion reactor which would operate on a pulsed cycle. Design studies over the years have identified many perceived shortcomings for operation of a pulsed tokamak reactor. These issues are concerned with the costs of thermal and electric energy storage, thermal fatigue in the blanket, first wall, and other high temperature components, and mechanical fatigue associated with oscillating magnetic fields. There was a measure of enthusiasm, therefore, when it was recently discovered that tokamaks can be operated in a purely steady-state mode, via continuous wave (CW) rf heating and current drive. The STARFIRE tokamak reactor study capitalized on the advantages of CW operation to demonstrate that such a fusion power plant could be economically competitive in producing electricity [1].

The principal concern with CW tokamak operation is the efficiency of generating the toroidal current by noninductive means. If a 10-MA toroidal current requires much more than 100 MW of auxiliary power absorbed in the plasma this may represent an unacceptable circulating power fraction and an unacceptably large capital cost for the driver. Unfortunately, experiments (e.g., PLT, Alcator C) are finding relatively small current generation efficiency for lower hybrid waves; scaling from present-day results, we would expect centrally peaked current density generation in a reactor with an efficiency, γ, of only ~0.01 A/W.

There are several proposals to improve this situation. Alternative drivers, such as the compressional Alfven wave, are theoretically superior to the lower hybrid wave, and one goal of this study is to quantify how large γ must be in order to make CW operation attractive. Another suggestion is to use noninductive drive only during low density periods, when the ratio of current to driver power, I_0/P_d, is large. (For all noninductive drivers $I_0/P_d \propto \gamma/\bar{n}_e$, where $\bar{n}_e$ is the volume average electron density.) One possibility here is to use noninductive current drive during such periods of low density operation, driving the current above the minimum value needed for fusion operation, and then permitting the current, I, to decay resistively during a brief period of high density fusion operation until the cycle must be repeated. This mode

[2-4], called internal transformer operation, completely eliminates the external transformer. Also, a hybrid cycle has been proposed [2,5] in which I remains constant, driven at high density during the fusion burn by an external transformer, and at low density by a noninductive driver while the tran ormer is reset.

The general purpose of our study is to gauge the benefits and costs of reactor operation under different burn cycle assumptions. We aim to determine reactor sensitivity to some uncertainties of plasma physics (resistivity, current drive efficiency). The various subsystems which we analyze include: first wall, limiter/divertor, breeder material and blanket structure, thermal energy storage, Ohmic heating (OHC) coils, equilibrium field (EFC) coils, toroidal field (TFC) coils, electrical power supplies, and noninductive driver systems. By assessing each subsytem's reliability and lifetime under different operating circumstances we attempt to quantify reactor performance characteristics for the various burn cycles.

In Sec. 2 we define the four burn cycles in more detail and identify operating windows for important factors such as magnetic field variations, thermal loads, dwell periods, etc. Also the models used for the sundry subsystems are presented. Much of the detailed subsystem analysis has already been documented in Ref. 6, and we summarize only the salient conclusions in the present report. Specifically, in Sec. 3 we discuss the implications of thermal fatigue for pulsed operation; goals for minimum fusion burn lengths are found. Whereas thermal fatigue limits the first wall and limiter lifetime, which affects reactor maintenance and availability, the effect of pulsed operation on magnets and energy handling requirements is reflected in the capital costs for these subsystems. Thus, in Sec. 4 we report the dependence of various capital costs on the reactor burn cycle parameters. Finally, in Sec. 5 we give a side-by-side comparison of tokamak reactors operating under different burn cycle assumptions and conclude with goals for tokamak research.

2. MODELS FOR BURN CYCLE ANALYSIS

2.1 Reference Reactor Systems

Two basic tokamaks are considered in our study. The "7-m reactor" has a major radius R_0 = 7.0 m and has a plasma quite similar to that in the STARFIRE

reactor [1]. This device has a small "hole in the doughnut" and serves as a model for the continuous (CW) burn cycle. The second tokamak, the "8-m reactor," was selected to characterize burn cycles with inductive current drive. This tokamak, with $R_0 = 8.0$ m, is by no means an optimized design but is merely indicative of the size needed to obtain fusion burns $\gtrsim 10^3$ s by inductive means. Both tokamaks have comparable fusion power, $P_f \approx 4000$ MW, and neutron wall loads, $W_n \approx 4$ MW/m^2.

Considering first noninductive current drive, we recall [7] that, for fixed beta, β_t, and fusion power, operation at high average plasma temperature ($\bar{T}$) reduces the density and therefore decreases the current drive power. However, the maximum toroidal magnetic field, B_M, must increase in order to keep P_f constant. This tradeoff is explored in Fig. 1 for the class of current drive techniques which add energy to electrons at suprathermal velocities. This "high-speed" drive is exemplified by lower-hybrid [8], magnetosonic [9], and electron cyclotron [10] waves and is characterized by an efficiency which scales as

$$I_0/P_d^{(0)} = (\gamma^{(0)}/n_{20})(7.0\ \text{m}/R_0) ,$$

where n_{20} is $\bar{n}_e$ in units of 10^{20} m^{-3}. In the best theoretical case (relativistic limit) $\gamma^{(0)} \approx 0.2$ A/W, whereas present-day experiments [11,12] report $\gamma^{(0)} \approx 0.017$ A/W. From the figure we see driver power is minimized by operating at $\bar{T}_e \gtrsim 12$ keV; there is also great incentive to achieve $\gamma^{(0)} \gtrsim 0.1$ since driver power in excess of 200 MW will be an expensive item if driver cost exceeds ~$1/W. The net electric power is plotted from the approximate formula $P_{net} = 0.357\ P_{th} - 73\ \text{MW} - (P_d^{(0)}/0.7)$, where the thermal power is due to alpha heating, the absorbed driver power, and neutron heating with blanket enhancement: $P_{th} = P_\alpha + P_d^{(0)} + 1.14\ P_n$. Also, we note P_{net} maximizes at $\bar{T}_e \gtrsim 12$ keV; $\gamma^{(0)} \gtrsim 0.06$ may suffice to achieve acceptable net power. The penalty for operation above ~12 keV is the rapid increase of B_M above 11 T. The credibility and reliability of such very high field TF magnets is called to question.

Low-speed wave drivers (Alfven [9], ion cyclotron minority heating [13]) as well as neutral beams [14] are characterized by current drive which scales as

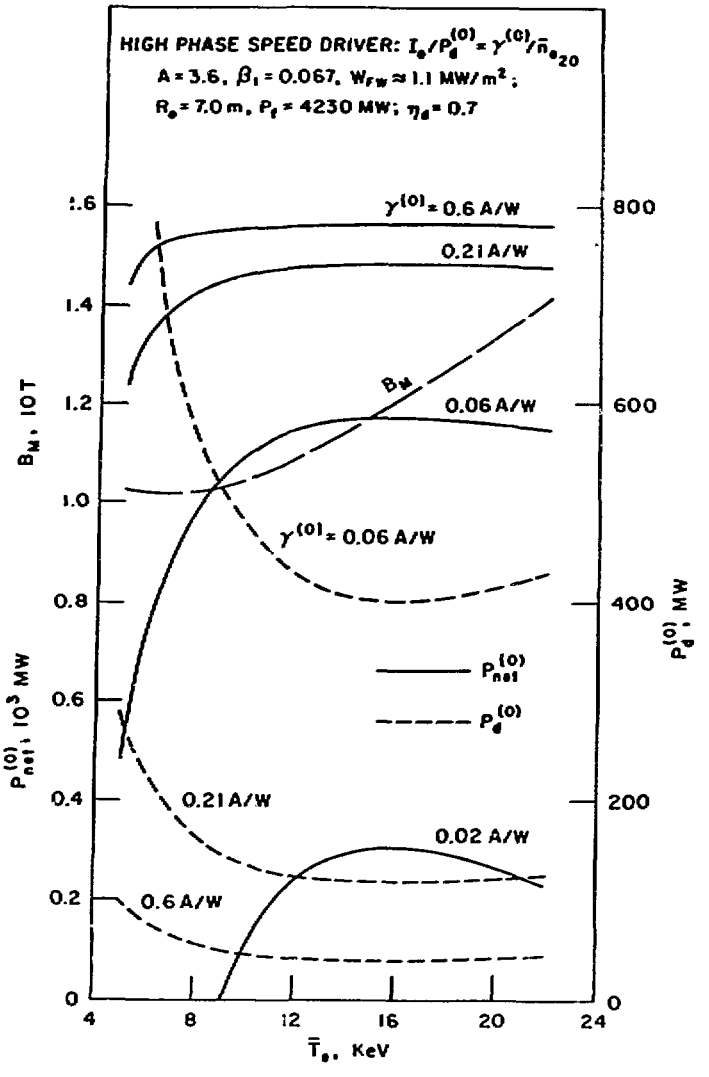

Fig. 1. High-speed current drive for various $\gamma^{(0)}$; required driver power, $P_d^{(0)}$, net electric output, $P_{net}^{(0)}$, and magnetic field, B_M, for R_0 = 7.0 m. Electric-to-current drive efficiency assumed to be η_d = 0.7.

$$I_0/P_d^{(1)} = (\gamma^{(1)}/n_{20})(\bar{T}_e/10 \text{ keV})(7.0 \text{ m}/R_0) ,$$

where $\gamma^{(1)}$ = 0.16 A/W in the best theoretical case [9]. The driver and net electric power are displayed in Fig. 2 for low speed drivers. The goals for γ

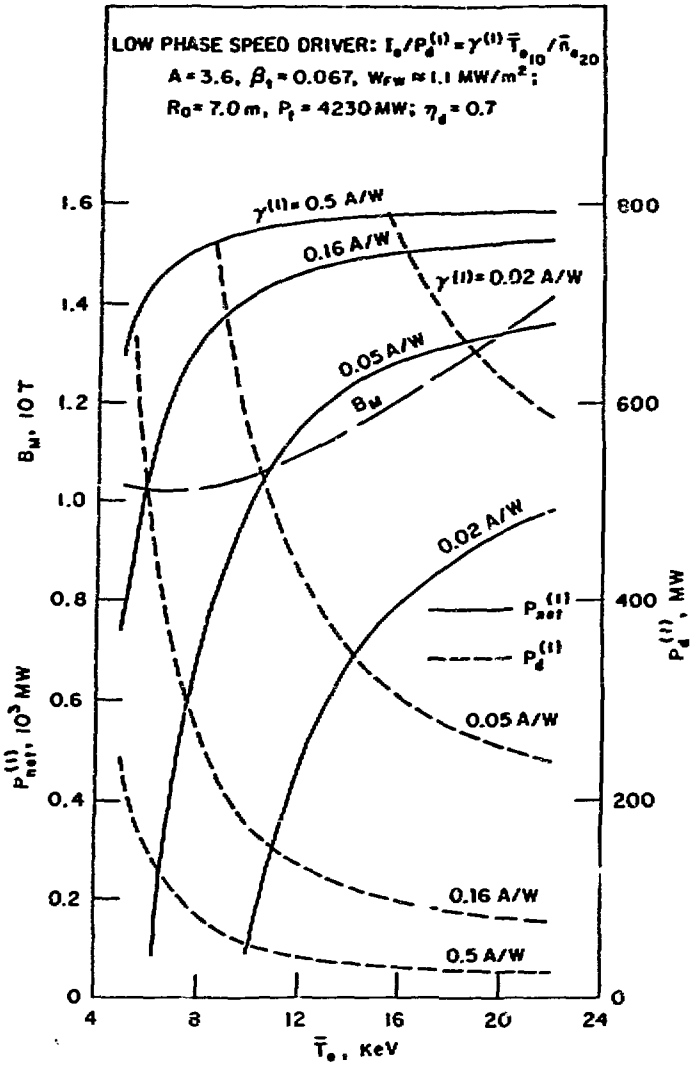

Fig. 2. Low-speed current drive for various $\gamma^{(1)}$.

($\gtrsim$0.1 A/W) and $\bar{T}_e$ ($\gtrsim$12 keV) are the same as above. For our study we assume the maximum practical fields are those obtained in the STARFIRE design [1], $B_M \approx 11$ T, so we select $\bar{T}_e \approx 12$ keV as the operating point for the 7-m reactor.

The selection of an optimum operating temperature for an Ohmicly driven tokamak involves the issue of burn length. Assuming plasma resistance drops with T_e we seek high temperature operation to maximize the burn length. How-

ever, the larger B_M needed to keep P_f constant as T_e increases beyond ~8 keV implies larger plasma current, I_0, to maintain MHD equilibrium. In addition, plasma resistance $\propto Z_{eff}$. Hence the loop voltage scales as the product $I_0 Z_{eff}/\bar{T}_e^{3/2}$. For the 8-m reactor at constant P_f we find this factor decreases rapidly until $\bar{T}_e \gtrsim 12$ keV and only slowly at higher $\bar{T}_e$. Countering this drop in loop voltage is a decrease in volt-seconds stored in the transformer of the reactor. At higher T_e the TF coils become thicker since B_M is getting larger. The result is a reduction in the size of the hole in the doughnut, R_{OH}, and in the transformer flux, $\Delta\phi_{OH,p} \approx \pi R_{OH}^2 \Delta B_{OH}$.

If we assume a transformer with field swing $\Delta B_{OH} = 2 \times 10$ T and a resistance close to Spitzer

$$R_{SP} = 2.2 n\Omega \times Z_{eff}[10 \text{ keV}/\bar{T}_e]^{3/2} ,$$

we find that the burn length, t_f, has a broad maximum, nearly 10^4 s, for 8 keV $\lesssim \bar{T}_e \lesssim$ 16 keV. In order to reduce the demands on the TFC we choose to operate at the lower end of this range, where B_M is relatively small. Our reference design operates at $\bar{T}_e = 10$ keV with $B_M = 9.8$ T, substantially lower than for the 7-m tokamak. Table 1 provides additional parameters of the two reference reactors.

2.2 Reference Burn Cycles

• Conventional ohmically driven (OH) cycle. This cycle is shown schematically in Fig. 3. The toroidal current is driven by a transformer, and once the volt-seconds are consumed the current decays and the fusion burn is extinguished. Both the current pulse, t_I, and fusion power period, t_f, are the same, ~10^3-10^4 s. Thermal loads and magnetic fields oscillate with the same periodicity. The figure illustrates single swing transformer action (plasma current and equilibrium field always in one direction), but double swing operation may be more attractive. Neutron power, P_n, and fusion thermal power, P_α, are zero when the plasma density, and temperature drop; during this down period, thermal power must be extracted from auxiliary storage units to supply the steam generators. Previous studies [15-17] of the OH cycle have addressed some issues related to the burn length.

TABLE 1

Reference Tokamak Reactors

Parameter	8-reactor	7-m reactor
Aspect ratio, A	4.0	3.6
Elongation, κ	1.6	1.6
Triangularity, d	0.2	0.2
Average beta, $\beta_t = 0.24/A$	0.060	0.067
Safety factor, q_{axis}-q_{lim}	1.0-2.5	1.0-2.5
Major radius, R_0	8.0 m	7.0 m
Inboard blanket/shield/scapeoff, Δ^i	1.4 m	1.4 m
Maximum field at TFC, B_M	9.81 T	11.2 T
Field at R_0, B_0	5.64 T	5.85 T
Toroidal current, I_0	13.0 MA	14.8 MA
Electron (ion) temperature, $\bar{T}_e(\bar{T}_i)$	10.0 keV (10.9 keV)	12.0 keV (13.9 keV)
Electron density, $\bar{n}_e$	2.02×10^{20} m^{-3}	1.90×10^{20} m^{-3}
Tritium density, $\bar{n}_T(=\bar{n}_D)$	0.719×10^{20} m^{-3}	0.696×10^{20} m^{-3}
Effective ion charge, Z_{eff}	1.70	1.80
Fusion power, P_f	3900 MW	4230 MW
Neutron power, P_n	3120 MW	3380 MW
Alpha power, P_α	780 MW	846 MW
First wall thermal (photon) power, P_{FW}	687 MW	704 MW
Current drive power (typical), P_d	0 MW	150 MW
Neutron wall load, W_n	3.5 MW/m^2	4.4 MW/m^2
Thermal power, $P_{th} = 1.14\ P_n + P_\alpha + P_d$	4337 MW	4849 MW
Gross power (100% D.F.), $P_g = 0.357\ (P_{th} + 33\ MW)$	1560 MW	1743 MW
Net power (nominal), $P_{net} = P_g - 85\ MW - (P_d/0.5)$	1475 MW	1356 MW
Plasma self-inductance, L	17.2 μH	14.1 μH
Spitzer toroidal resistance, R_{SP}	3.69 nΩ	2.74 nΩ

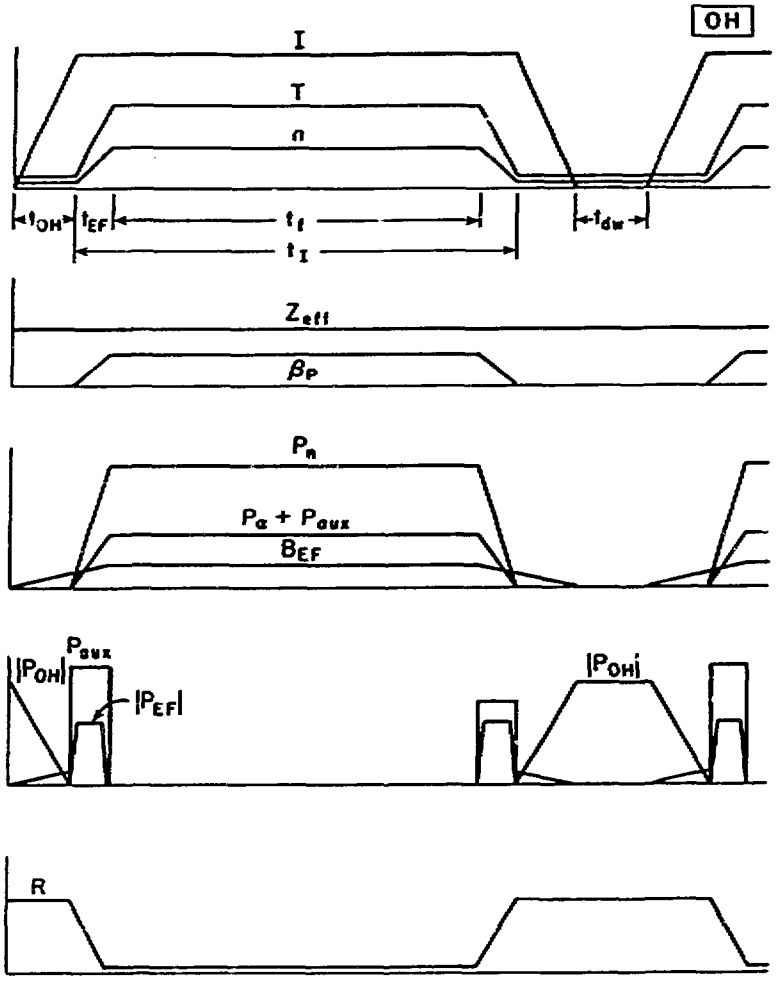

Fig. 3. Schematic OH cycle. Auxiliary power, P_{aux}, is used for heating to ignition during period t_{EF}. Startup and shutdown ramps are nearly symmetric.

• Continuous (CW) operation. This technique [1,18] is only practical if noninductive current drive is sufficiently efficient during high density fusion operation that the circulating power, P_d, is a small fraction of the fusion power. With this proviso, however, reactor operation is possible in principle for very long periods (months), until reactor maintenance forces shutdown. Fatigue is expected to be of minor concern since only a few hundred

thermal and magnetic cycles occur in the reactor lifetime. Thermal storage is eliminated, slow current and power ramps minimize the cost of startup power supplies, disruptions may be very infrequent, and additional design latitude derives from eliminating the external transformer.

- Internal transformer (IT) operation. This mode of operation [2-4] requires no external transformer. Instead, noninductive current drive is used during periodic low density phases to boost toroidal current by a small increment ΔI (see Fig. 4). Between current drive periods the density is increased for full fusion power production, and the current decreases resistively for a burn length $t_f \approx \Delta t_I \approx (\Delta I/I_0)(L/R)$. If we keep the toroidal current nearly constant $(\Delta I \ll I_0)$, the burn is limited to a relatively short period ($\sim 10^2$ s), and this mode will result in many times more total fusion cycles in the reactor lifetime than the OH cycle. The fusion power oscillations lead to thermal cycling, as in the OH cycle. The equilibrium field, B_{EF} will also fluctuate; even though toroidal current is nearly steady, poloidal beta, β_p, fluctuates from density cycling. We can expect B_{EF} variations on the order of half the full field value, for a typical IT cycle.

- Hybrid transformer operation. A variation from the IT cycle, this would use an external transformer to maintain I_0 during the fusion burn and then keep I_0 at full value with low density noninductive current drive while the transformer is quickly recharged [2,5]. As with the IT, both thermal and magnetic fluctuations occur, but the fusion period is much longer, resulting in fewer lifetime cycles. Compared to the OH cycle this mode benefits from keeping I_0 constant: equilibrium field power, P_{EF}, may be smaller, downtime may be shorter, periodic purging and plasma breakdown is avoided, and disruptive regimes might be circumvented. The burn cycle wave forms are similar to those in Fig. 4, except that the toroidal current remains constant (for many months, in principle) and with the addition of a power supply (P_{OH}) which charges the OHC during the dwell period.

2.3 Subsystem Models and Performance Analysis

For our studies we consider multiple concepts for most subsystems in order to reflect the uncertainty of future technology.

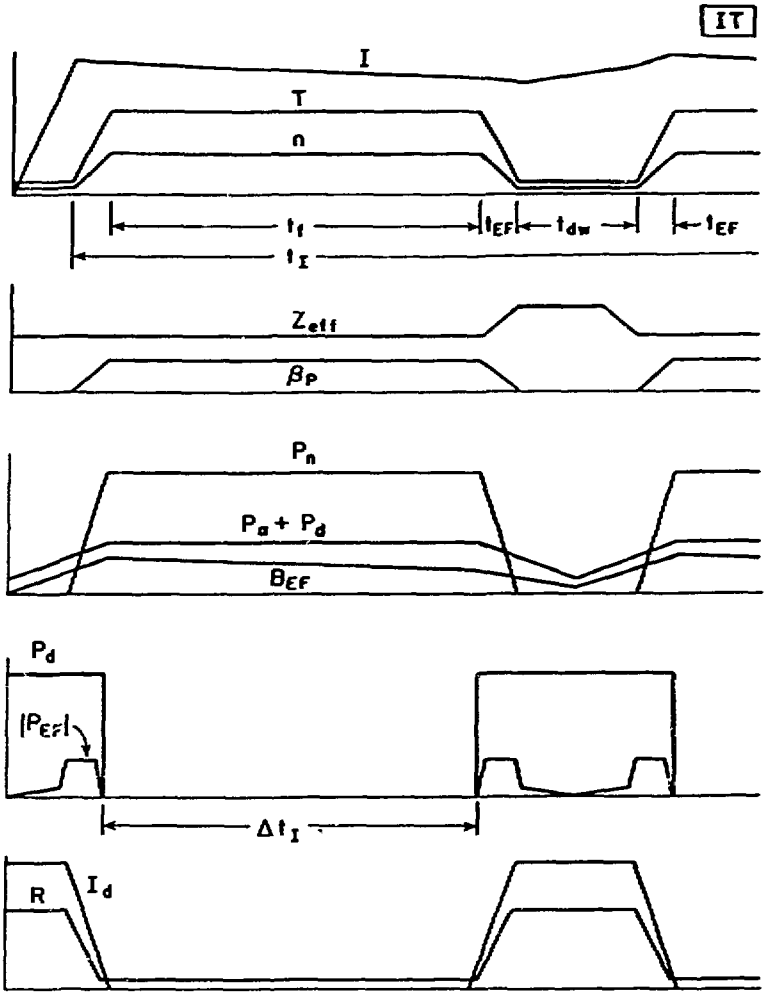

Fig. 4. Schematic internal transformer cycle. Driver power, P_d, is used only during dwell, t_{dw}, to increase toroidal current, I; plasma resistance, R, is made to increase during dwell by enhancing Z_{eff}.

In the case of the limiter structure we have studied two basic alternatives. One system, representative of near-term technology, has a copper alloy for the heat sink structure and is water cooled (4 MPa, 130°C). A more advanced alternative has a vanadium alloy heat sink with liquid lithium coolant (4 MPa, 210°C). The actual geometry is that proposed and analyzed in the

STARFIRE study [1]. The front face of the limiter (that portion closest to the plasma) is modeled as a flat slab with a thermal load, W_{ff} = 1.5-3.5 MW/m^2, and the leading edge is analyzed as a cylinder. Careful design of the limiter geometry is expected to result in leading edge thermal loads smaller than those on the front face; we consider W_{le} = 0.75-1.75 MW/m^2. For this study we assume the entire limiter is laminated with a surface material (tiles) specifically designed to reduce sputtering poisoning of the plasma [19]. The high plasma temperature at the front face constrains our choice to a small class of options, and we pick beryllium as a typical coating. Near the leading edge the plasma temperature is lower, and a larger number of options are possible, and we consider both beryllium and tungsten as coatings.

The first wall is treated as a simple bank of cooling tubes [20]. One option is water cooled (15 MPa, 300°C) with prime candidate alloy (PCA) for the tube structure. We use 20% cold worked 316 stainless steel to model the PCA properties. At these high pressures a thin wall tube requires a small inner radius, and we consider r_1 = 3-10 mm. The more advanced design utilizes liquid lithium (2 MPa, 350°C) as a coolant and vanadium as the structure. The low pressure permits relatively large radius piping; r_1 = 25 cm is chosen. The surface heat load W_{FW} = 0.5-1.0 MW/m^2, is due mainly to photon radiation, so the first wall is taken to be bare structure.

Electric power supplies are needed to transfer energy to magnets. The systems in this study are based on current technology, since this was found to be the least expensive option. The EF coils are powered through a silicon controlled rectifier (SCR) assembly from a motor-generator-flywheel (MGF) set. A similar power train is used to reset the OH coil between fusion burns of the ohmically driven and hybrid burn cycles. A third power system is needed for the ohmic burn cycle in order to supply high loop voltage for startup; this power supply dumps considerable energy from the OHC through a resistor. The dump resistor operates with very high power transients but is relatively inexpensive.

The pulsed superconducting magnets (the OHC and EFC) as well as the TF coils utilize the multifilament cable described in the STARFIRE design [1]. Only niobium-titanium was considered for the OHC since the pulsed nature of its operation would make Nb_3Sn a poor alternative.

The TFC model is a critical input to this burn cycle study since the TFC is a very expensive system and is sensitive to fatigue from out-of-plane bending. Our focus is on one particular TFC design, described in the STARFIRE study [1]. The superconductor is housed in a helium vessel at 4.2 K which is suspended by thin struts (of low thermal conductivity) from an enclosing room temperature vacuum tank. Both vessels are constructed from Type 316 LN stainless steel (annealed). The overturning moments on the TFC are resisted by the steel support cylinder (inboard) and shear panels (outboard). This leaves unsupported free spans, along the top and bottom legs of each TFC, which are restrained from gross bending by the stiffness of the vacuum tank. (Alternative TFC structures with additional intercoil supports may offer cost advantages at the extremes of high cycle fatigue but have not been explicitly studied.)

Fatigue damage to reactor structure is due to both fluctuating electromagnetic forces and varying thermal expansion and is studied with two distinct methods. Thin structures (steel bands in the magnets) and cooling tubes designed for high static primary pressures are analyzed with smooth sample data curves which show the number of cycles to failure versus the strain variation per cycle. Thick structural members (in the TFC system), on the other hand, are assumed to have flaws which are initially present but undetected due to the thickness of the structure. Prudence then dictates that a crack propagation analysis be undertaken for estimating lifetime.

Besides thermal fatigue, the first wall and limiter experience high heat loads, and, based on previous fusion materials studies [19,21,22], appropriate temperature limits have been imosed for the various coatings and heat sinks. These constraints reflect the life-limiting effects of high temperatures on radiation-induced swelling, tensile strength, ductility, and thermal creep. Another life limit to plasma-exposed components is the thermal damage from major disruptions. The primary parameters are the energy deposition per unit area, the thermal dump duration, and the frequency of disruptions. Extrapolating from INTOR [19] we expect maximum energy densities of ~800 J/cm^2 on the first wall and ~2500 J/cm^2 on the limiter. The resulting vaporization and melt layer thickness are found for the candidate materials using the A*THERMAL code [23] for several disruption times. For this burn cycle study we have adopted one particular model for the frequency of disruptions, namely, that

their occurrence correlates with the number of fusion burn cycles. (This is expected if disruptions are initiated by transient plasma conditions, such as current density and pressure profiles.) Thus the prevalence of disruptions is treated statistically, and we examine probabilities of f = 10^{-2}, 10^{-3}, and 10^{-4} disruptions per burn cycle.

Radiation effects are included as follows. The first wall heat load (mostly photons) is $W_{FW} \approx W_n/4$, the limiter's leading edge experiences $W_{\ell e} \approx 0.4\ W_n$ and the front face has $W_{ff} \approx 0.8\ W_n$, where W_n is the neutron wall load. In the thermal analysis of coatings and structure nuclear bulk heating is included. Based on a survey of swelling and loss of ductility under radiation conditions we assign these life limits, L_{rad}, for neutron fluence to structural materials: Cu = 4 MW-y/m^2; PCA = 12 MW-y/m^2; V = 24 MW-y/m^2. Radiation-induced creep is felt to be less damaging than thermal creep, and values as high as 5% are assumed acceptable in our stress analysis.

The total number of fusion cycles in the reactor lifetime is based on a 40-y assumed lifetime and 80% availability (1.0×10^9 s of operation). Our philosophy is that all burn cycles must achieve this high availability to be of interest to a utility. We attempt to calculate burn cycle requirements and system capital costs needed to approach these goals. All costs are in 1983 dollars. An accurate estimate of subsystem reliability, mean time to replace failed components, and system availability is obviously not possible at present. However, the data presented here provide a useful comparison of the relative attractiveness of the various burn cycles to different reactor subsystems.

3. FIRST WALL AND LIMITER LIFETIME

Our aim is to maximize component lifetime against simultaneous failure modes. First, thermal fatigue is calculated, and we find that cycle life generally decreases for thicker structures and coatings. Next we study material loss from disruptions and show how component cycle life increases with thicker structures and coatings. The component dimension corresponding to the intersection of these life curves is considered optimum for obtaining the longest cyclic life. Then the minimum fusion burn length is found such that the total cyclic life is not shorter than the expected component life against radiation damage. (Erosion due to sputtering is not extensively examined as a

life limit; we assume that net sputtering erosion must be made insignificant either through proper plasma edge conditioning or, for example, via periodic resurfacing techniques.)

3.1 Thermal Fatigue

A thermal-hydraulics analysis was done to provide temperature distributions in the coatings and structural materials. These results are used as input to the stress analysis and to ascertain that temperatures are within the acceptance levels. One-dimensional steady-state calculations are performed. We find that, for a given heat sink thickness in the limiter, surface temperatures increase with the thickness of the coatings as well as with the thermal heat load, as expected. The leading edge, due to its cylindrical geometry, experiences rising temperatures also in the heat sink as the coating thickness increases [19].

For design purposes a safety factor of two on strain or twenty on cycles is applied to the fatigue crack initiation curves of the various structural materials [6]. As an example, Fig. 5 shows the fatigue life of beryllium-clad copper as a function of the coating thickness and surface heat flux at the leading edge. In general, the fatigue life decreases with increasing coating thickness and increasing surface heat flux. Beryllium-coated copper has longer life than tungsten-coated copper. For small coating thicknesses ($\lesssim$1 cm), the use of a stronger copper alloy (e.g. AMAX-MZC) instead of pure annealed copper can increase the design fatigue life significantly. For the alternative heat sink alloy (V-15Cr-5Ti), we find, in general, the fatigue life of vanadium is much greater than for copper. Except for small coating thicknesses ($\lesssim$2 mm), beryllium-coated vanadium has longer fatigue life than tungsten-coated vanadium.

The top surface of the limiter is analyzed as a flat plate constrained to deform with the cooler back part of the limiter. The fatigue life of both copper and vanadium heat sinks, as functions of beryllium coating thickness and surface heat flux, was calculated. Despite higher surface heat loading, the cyclic life of the top surface is comparable to that of the leading edge.

Figure 6 shows the plot of cyclic life versus first wall tube thickness for various thermal wall loads on a tube of 316 stainless steel with an inner radius of 5 mm. Also shown in this figure (by open circles) are the maximum

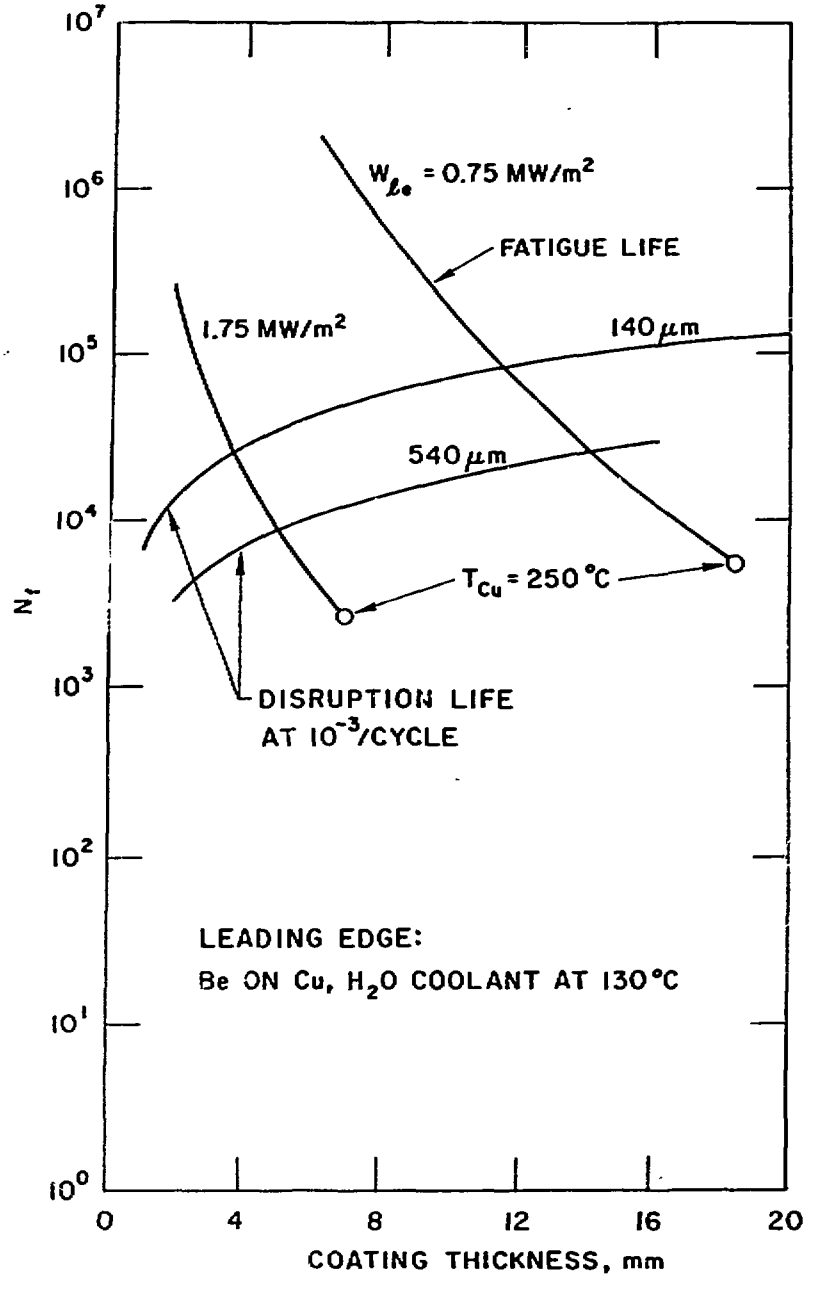

Fig. 5. Leading edge cyclic life versus fatigue and disruption erosion.

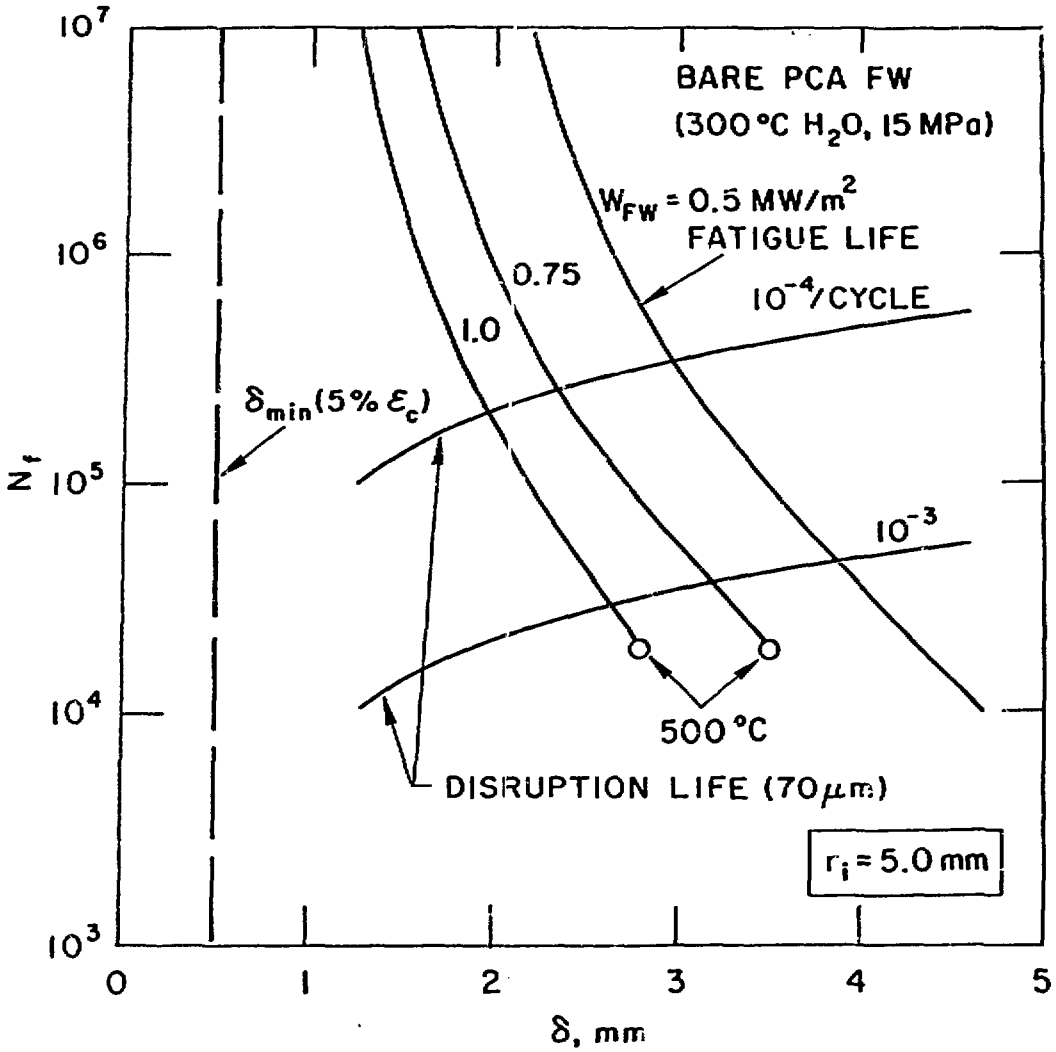

Fig. 6. First wall cyclic life versus fatigue and disruption erosion; minimum pipe thickness to withstand rupture, δ_{min}, is set by 5% radiation-induced creep strain.

thicknesses corresponding to a maximum allowable metal temperature of 500°C. The fatigue curves and the maximum temperature limit give upper bounds to the wall thickness for a given surface heat flux. A lower bound for the wall thickness is set by the primary stress criterion, $P_m \leq S_{mt}$. The figure shows minimum thickness corresponding to a time-dependent stress limit S_{mt} corresponding to a maximum radiation-induced creep strain of 5%. The difference between the lower bound and the upper bound for thickness may be considered as the margin against erosion.

Similar plots were made for the case of V-15Cr-5Ti with a tube of radius 25 cm. In this case the maximum metal temperature limit of 600°C sets an upper bound for the vanadium first wall thickness. Because of their superior thermal properties vanadium tubes can have significantly larger wall thickness (6-10 mm) and longer cyclic lifetime ($N_f \gg 10^6$) than 316 stainless steel tubes.

3.2 Erosion from Disruptions

Figure 7 shows the total material erosion as a function of disruption energy density for both first wall and limiter materials. Vanadium as a first wall material results in much less erosion than stainless steel. At these energies the main material erosion is from melting. For limiter coatings, beryllium shows much higher erosion than tungsten. The threshold energy density to induce melting in beryllium is near 350 J/cm^2 while for tungsten it is about five times higher. This is mainly because of the very high melting point of tungsten.

Note that the material loss is quite sensitive to the energy density. If steps can be taken to reduce disruption energy densities by a factor of two from the worst cases shown, then significant reductions in damage can result. Likewise, if the melt layer is stable and only vaporized material is actually lost, then erosion can be less significant.

3.3 Lifetime Analysis and Burn Goals

We begin by considering the limiter's leading edge, and we first consider the copper heat sink with water coolant and a beryllium coating (Fig. 5). As previously stated, fatigue life increases with thinner coatings. However, thinner coatings are more easily eroded by repeated disruptions. From Fig. 7 we might expect up to 540 μm of beryllium removal per disruption near the upper limits of leading edge thermal dumps (~1000 J/cm^2). Hence the beryllium coating, with thickness δ_{Be}, can be removed in the worst case after a number of fusion cycles $N_f = \delta_{Be}[f \times 0.54 \text{ mm}]^{-1}$, where f is the average frequency (probability) of disruptions per burn cycle. Figure 5 displays N_f versus δ_{Be} for $f = 10^{-3}$ (one disruption per thousand burn cycles) and two different coating removal rates. The optimum coating thickness is the intersection of fatigue and disruption curves. For example, for high leading edge heating,

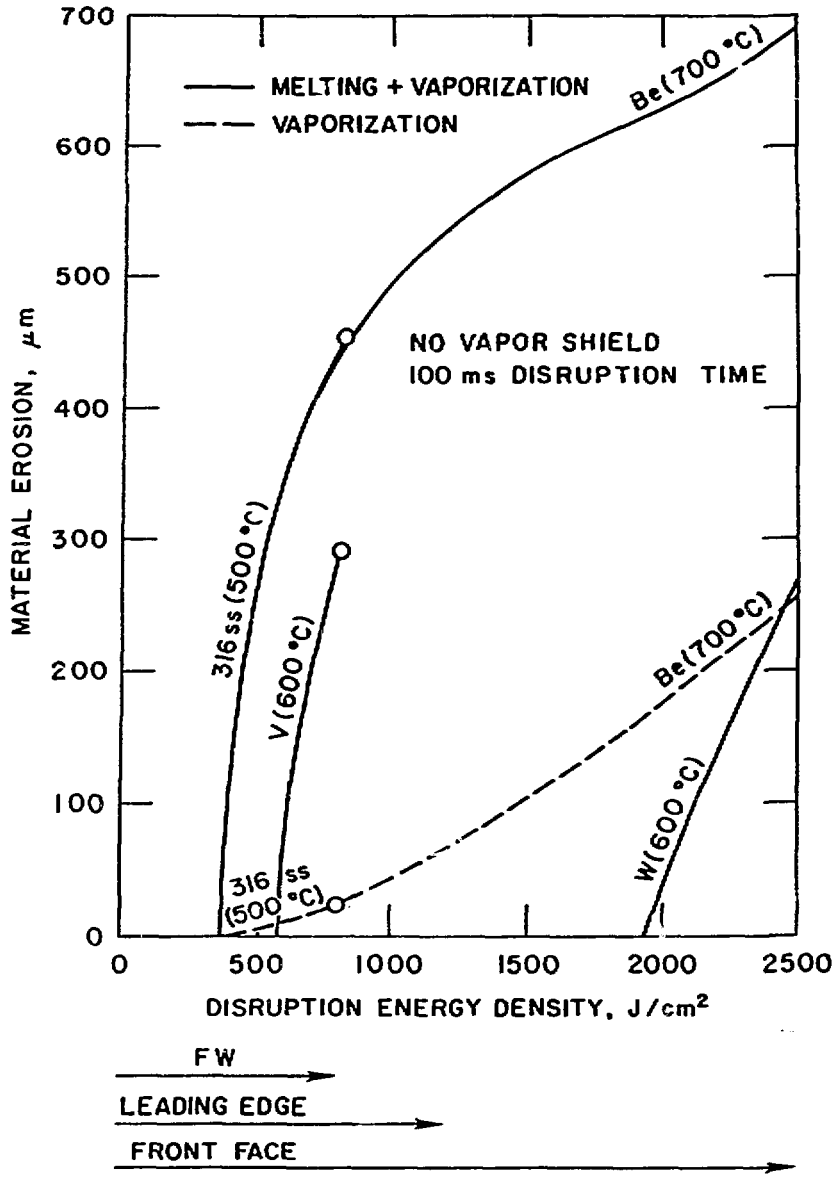

Fig. 7. Disruption damage.

1.75 MW/m^2, and mild disruption damage, 140 μm lost per disruption, the maximum lifetime is to be expected for δ_{Be} = 3.6 mm, which results in a survival time of $N_f = 2.7 \times 10^4$ burn cycles.

Finally, we fold into our analysis the radiation life limit for the heat sink. Our philosophy will be that the fusion burn length, t_f, should be long enough that the cycle life, N_f, is at least as long as the radiation life. Thus, we compute the minimum

$$t_f = \frac{L_{rad}}{W_n N_f} - 100 \text{ s} ,$$

where we assume a 100-s lapse between burns. As an illustration, the copper heat sink is believed to have poor radiation resistance, $L_{rad} \approx 4$ MW-y/m^2; at a neutron wall load of $W_n = 4$ MW/m^2 one might expect to require its replacement every year. Then, a fusion period $t_f = 1.1 \times 10^3$ s would be needed in order for a cyclic lifetime $N_f = 2.7 \times 10^4$ to equal the radiation lifetime. Figure 8 shows these burn goals for the beryllium/copper leading edge under different conditions. In the case of severe disruption damage there is a strong motivation to achieve $t_f \approx 1$ h. The motivation for long burns diminishes for more mild disruptions. In fact, according to Fig. 7, disruptions do no damage at thermal loads $\lesssim 300$ J/cm^2, so very thin coatings with negligible fatigue could be selected in this limit. The first lesson we have learned is that $t_f \approx 1$ h may be adequately long to eliminate fatigue as a life-limiting consideration if the limiter leading edge has a heat sink with poor radiation resistance. This set of circumstances might typify a near-term tokamak constructed with conventional technology (water-cooled copper heat sink). At 80% availablity we note the limiter calendar lifetime is $T = L_{rad}/(W_n \times 0.8)$. T is indicated by the tick marks on the curves in Fig. 8 and is relatively short (~1-2 y) for the copper structure.

It may well be that a commercial reactor would be designed with more radiation resistant materials in order to extend the period between limiter repairs. As an example we consider a vanadium heat sink at the leading edge, clad with beryllium. The superior fatigue resistance of vanadium results in a much longer cyclic life than the copper heat sink. For moderate damage rates, disruptions are the life-limiting concern, so δ_{Be} should be maximized to the temperature limit. The corresponding number of burn cycles can again be converted to a burn length such that the cycle lifetime at least equals the radiation lifetime. For vanadium, however, radiation resistance is believed to be much better than for copper (we take $L_{rad} = 24$ MW-y/m^2) The results are shown

in Fig. 8. Compared to a copper heat sink there is strong motivation to achieve longer burns. For severe disruptions burn times exceeding 3 h are desired. These longer burns are needed in order to achieve the full potential radiation life of the limiter, in the range of seven to fifteen years.

In the desirable situation where disruptions can be completely eliminated from tokamak reactors we must consider sputtering as an erosion mechanism. In Fig. 8 we illustrate the burn cycle implications with $\dot{\delta}_{Be}$ = 1 cm/y. Since sputtering life is so short, radiation damage does not concern us in this limit. The beryllium coating is increased to the temperature limit to maximize life against erosion, and the number of acceptable fatigue cycles is found. For the copper heat sink N is now smaller than for the cases dominated by disruptions so a longer t_f ($\gtrsim$3 h) is needed to obtain a 1-2 y lifetime of the leading edge; for the vanadium substrate N_d is now larger, so a shorter t_f ($\lesssim$100 s) is permissible.

Tungsten has also been proposed as a limiter coating at the leading edge. If the plasma temperature exceeds ~50 eV at the leading edge the high net sputtering of tungsten will preclude its use. However, at lower temperatures this appears to be an ideal coating. Sputtering is then low and redeposition is very effective due to the short mean free path of tungsten ions. In addition, disruptions do little damage to a tungsten coating since, at the leading edge, the thermal load is likely to be less than the threshold for melting and vaporization; see Fig. 7. Hence, at such low temperatures erosion may not be significant for tungsten coatings. A thin tungsten cladding, δ_W, would be specified. Since our fatigue calculations show very large cycle lifetimes for either copper or vanadium substrates with $\delta_W \lesssim 1$ mm we find that fatigue may not be an issue for the leading edge whenever a tungsten cladding can be used.

An identical lifetime analysis was done for the front face of the limiter. The beryllium coating was assumed to be removed at 690 μm and 170 μm per disruption, representing the worst case and more mild disruption damage (2500 J/cm^2 and 500 J/cm^2, respectively). The optimum δ_{Be} was inferred for a disruption probability $f = 10^{-3}$, and the minimum t_f results are displayed in Fig. 9. Our first observation is that $t_f \approx 1$ h is adequate for the front face with a copper heat sink, even with the worst disruption damage. However, the one- to two-year radiation life of copper is so short that there will be great incentive to consider materials such as vanadium. Then we find, in order to

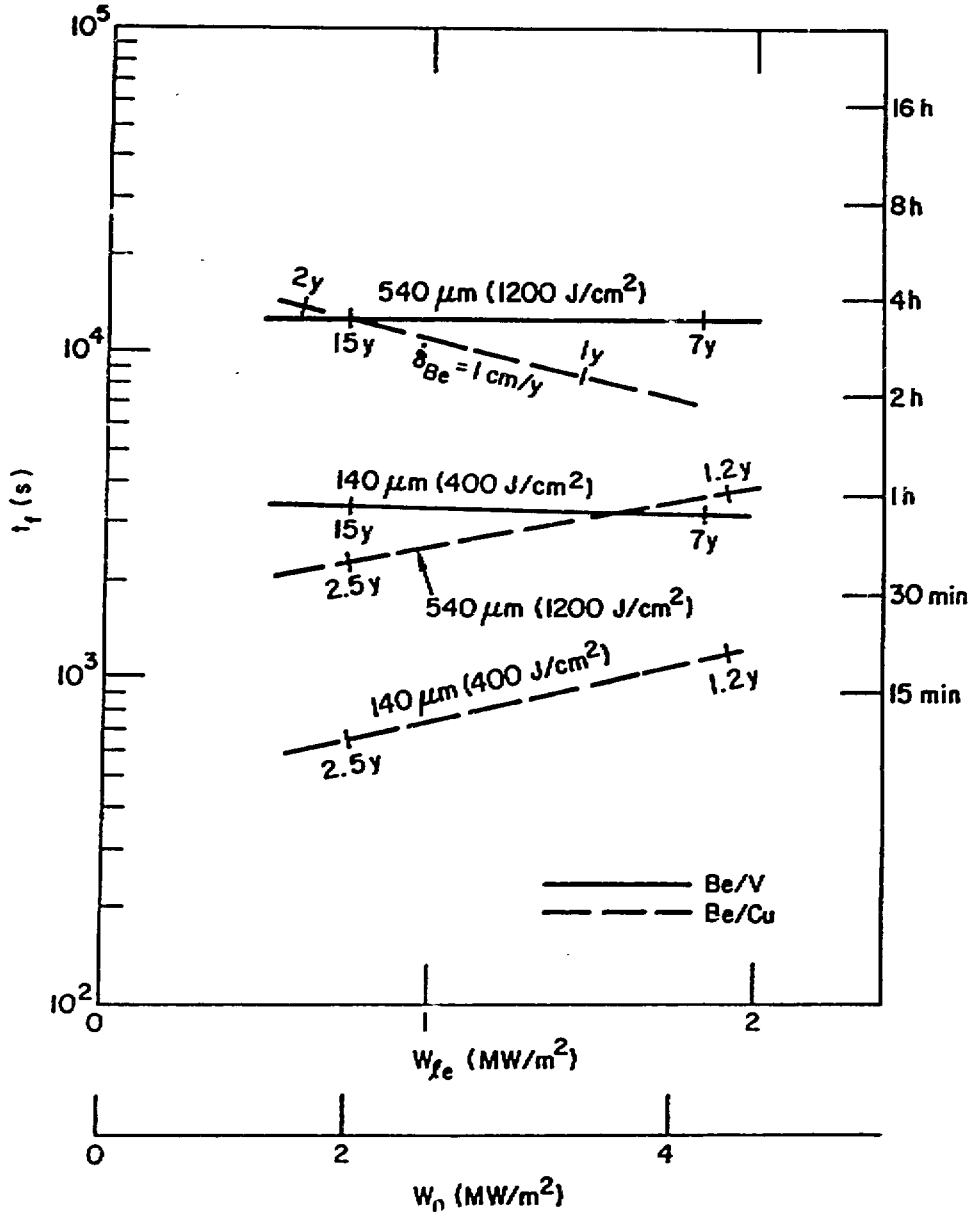

Fig. 8. Fusion burn length goals to maximize limiter's leading edge life against fatigue, disruptions, radiation and sputtering. Disruption frequency is assumed to be $f = 10^{-3}$ disruptions/cycle with no net sputtering, except for $\dot{\delta}_{Be} = 1$ cm/y sputtering curve, which assumes $f \equiv 0$. Component replacement interval is indicated along the curves.

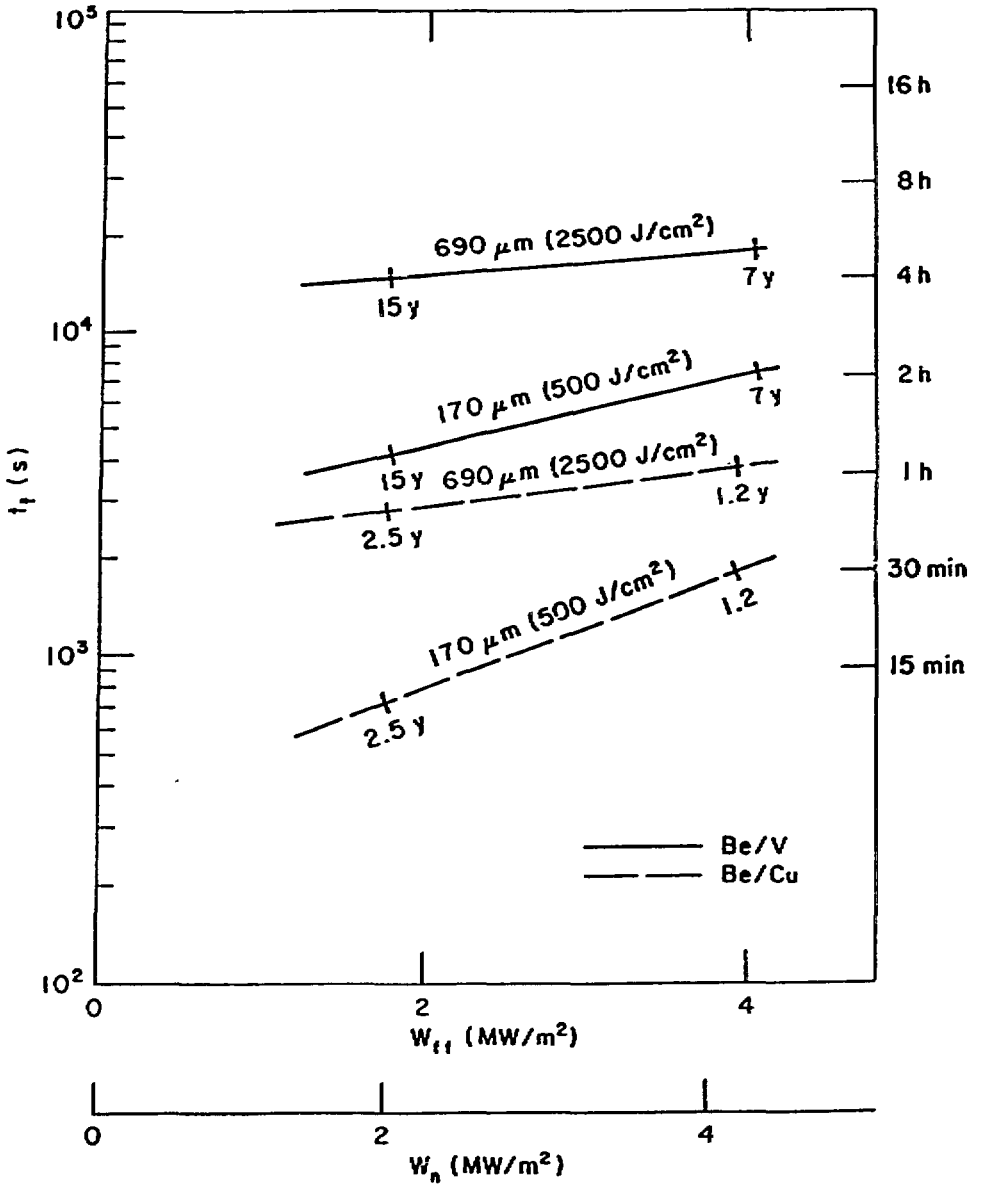

Fig. 9. Fusion burn goals to equate cyclic and radiation life of limiter's front face; no sputtering; f = 10^{-3} disruptions/cycle.

achieve the six-fold increase in limiter life, the burn length must be extended so as not to aggravate the fatigue problem. For moderate disruptions we need $t_f \sim$ 1-2 h. Of course, if the frequency of disruptions were f << 10^{-3} then thinner beryllium coatings, with resulting longer fatigue life for

the substrate, would be appropriate. In the extreme where sputtering erosion limits the lifetime to ~1 to 2 y the burn length would need to be only 15-30 min in order to eliminate thermal fatigue as a concern with a vanadium substrate.

We next analyze the first wall lifetime, starting with the bare PCA water-cooled tubes. In Fig. 6 we display the cycle lifetime against disruptions for f = 10^{-3} and 10^{-4}, assuming modest thermal energies in the disruption (380 J/cm^2 removing 70 μm of PCA). The tubing is assumed to fail once disruptions thin the wall to $\delta_{PCA} = \delta_{min}$. Thus, for 70 μm loss per disruption we find a disruption controlled cycle lifetime of $N_f = (\delta_{PCA} - \delta_{min})(f \times 0.07 \text{ mm})^{-1}$. As with the limiter we select the intersection of the fatigue and disruption curves to find the δ_{PCA} which yields the maximum cycle life, N_f, and we compute the fusion burn period needed for the cycle lifetime to equal the radiation life, (with L_{rad} = 12 MW-y/m^2). The results, shown in Fig. 10, indicate that relatively short burns, t_f ≈ 1 h, suffice to eliminate the cycling factor from concern when there are infrequent or mild disruptions. It is conceivable that the disruption damage could be more troublesome, however. Merely increasing the energy deposition from 380 J/cm^2 to 700 J/cm^2 multiplies the melting and vaporization loss by a factor of six for PCA (see Fig. 7). This motivates a design goal for much longer fusion burns; as shown in Fig. 10, t_f ≈ 5 h is needed to realize the full radiation life potential in this case.

Finally, we consider the burn goals needed to achieve the full benefits of radiation resistant structure such as vanadium. The 600°C creep limit on vanadium constrains δ_V to ≲10 mm, and we find disruption erosion dominates fatigue as a consideration. Our results, displayed in Fig. 10, show that t_f may be as long as that required for the PCA first wall in order to achieve twice the in-reactor lifetime (8-14 y versus 4-7 y). In the pessimistic disruption scenario depicted we find t_f ≈ 8 h is desirable at high wall loads.

We conclude this section with some general observations. Our results typically show that "near-term" structures such as copper limiters and a steel first wall can tolerate relatively short fusion burns because their radiation life is thought to be short. In order to take full advantage of advanced materials with longer radiation life it will be necessary to arrange for longer burns (CW or long pulse operation). On the other hand, reactors with

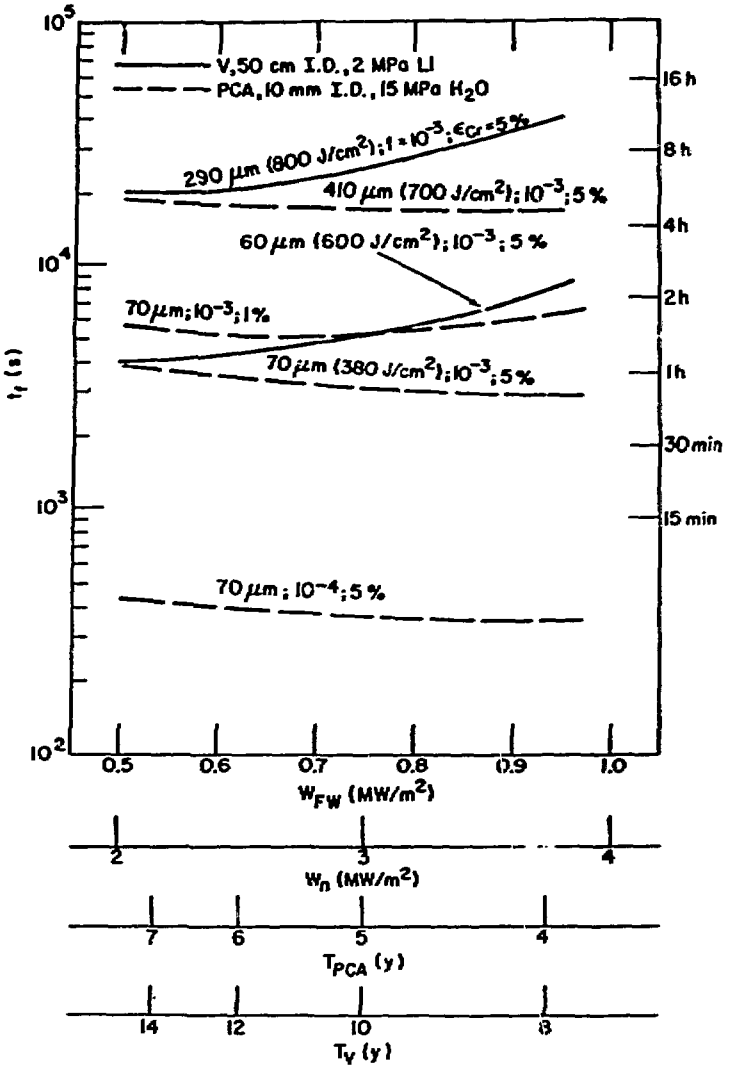

Fig. 10. Fusion burn goals to equate cyclic and radiation life of first wall; sputtering is negligible. Component replacement interval is given by lower abscissas.

short burns ($t_f \sim 100$ s), operating in the internal transformer mode, will not be attractive unless disruption frequency is $f \lesssim 10^{-5}$ and sputtering erosion is $\dot{\delta} \lesssim 1$ cm/y.

Generally speaking, the higher thermal loads are more demanding on our designs. In the first place this is because we have assumed the higher thermal loads are associated with higher neutron damage and therefore shorter in-

reactor life. In the second place these higher thermal loads exacerbate the fatigue problem and generally require longer burns in order to not surpass the limit on cycle lifetime.

Finally, we caution that our results only display general trends. Reactor availability should improve with several factors: use of more radiation and fatigue resistant materials; reduction in the frequency and severity of disruptions; reduction in net sputtering erosion; selection of disruption resistant materials; operation at lower wall loads; as well as operation with longer fusion burns.

4. CAPITAL COST SENSITIVITY TO BURN CYCLES

4.1 Ohmic Heating Coil

The transformer can be an expensive, high energy component for reactors employing the OH or hybrid burn cycles. The first question we address, then, is how to optimize its design. In particular, we examine several options for the 8-m reactor in order to select the maximum practical solenoid field, B_{OH}. The designs are summarized in Table 2.

In formulating costs for magnets we note that there is often wide disagreement in cost estimates for these items, as would be expected for an industry which is still in its infancy. Therefore, we estimate costs on two different bases. If we consider current material costs and fabrication techniques [24] we find fairly expensive magnet costs; including wire and cable production, fabrication, and winding we estimate this as

$$C_I = m_{Cu} \times \frac{\$157}{kg} + m_{NbTi} \times \frac{\$460}{kg} + m_{SS} \times \frac{\$30.1}{kg} ,$$

where m_i is the required mass of the various magnet materials. However, if tokamak reactors are commercialized we would expect significant price reductions due to mass production and learning experience. According to Ref. 1 we can predict future technology to provide

$$C_{II} = m_{Cu} \times \frac{\$34.4}{kg} + m_{NbTi} \times \frac{\$118}{kg} + m_{SS} \times \frac{\$16.7}{kg} \times m_{NbSn} \times \frac{\$234}{kg} ,$$

TABLE 2

Design Options for OHC Central Solenoid

Parameter				
Maximum field, B_{OH} (T)	8	10	10	12
Helium temperature (K)	4.2	4.2	1.8	1.8
Critical current density in NbTi (kA/cm^2)	70	29	200	70
Actual current density in NbTi (kA/cm^2)	38	20	80	35
Average current density in winding (A/cm^2)	1225	1080	1320	1050
Radial build of winding, Δ_{OH} (m)	0.52	0.75	0.61	0.93
Mean radius, R_{OH} (m)	2.78	2.66	2.72	2.56
$2\pi R_{OH}^2 B_{OH}$ (V-s)	387	445	465	494
Average heat generation (8000-s cycle) (W)	63	213	53	104
NbTi mass, m_{NbTi} (Mg)	28.8	65.6	16.8	43.6
Copper mass, m_{Cu} (Mg)	170	220	176	215
Steel mass, m_{SS} (Mg)	273	428	484	613
Winding cost, near-term, C_I ($M)	48.2	77.6	49.9	72.3
Winding cost, long term, C_{II} ($M)	13.8	22.5	16.1	22.8

Designs based on: 50-kA cable; stainless steel structure at 500-MPa stress (S_m for 316 LN); solenoid length = 15.4 m; $\dot{B}_{OH}$ = 0.2 T/s; 1983 dollars.

where we have included Nb_3Sn as a possible superconductor. These costs are included in Table 2.

We see from the table that as B_{OH} increases from 8 T to 12 T the volt-second rating increases at a slower rate, by only 27%. This is due to the increased radial build, Δ_{OH}, of the solenoid at higher fields, which decreases R_{OH}. Considering the increased costs and lower critical current densities near the 12-T range, we feel a practical design goal for the solenoid is this about 10 T, which concurs with previous studies [17]. Significant benefits (high current density) accrue from selecting 1.8 K cooling at 10 T, rather than 4.2 K, and we therefore select the 1.8-K design for the reference OHC.

Two additional outer ring coil sets complete the OHC magnetic system. These windings are in relatively low fields (~3-7 T) and employ 4.2-K pool boiling. The actual flux coupled to the plasma current is $\Delta\phi_{OH,p}$ = 444 V-s,

slightly less than the 465 V-s of the ideal infinite solenoid. These ring coils require 12.3 Mg of NbTi, 101 Mg of copper, and 276 Mg of steel if a stress level of 500 MPa is permitted; this represents additional winding cost of C_I = \$29.8 M or C_{II} = \$9.5 M. We estimate the helium vessel to cost ~\$3.1 M for the whole OHC system.

We find, thus, there is a cost penalty of at least ~\$30-80 M for any burn cycle requiring a full OHC system. Moreover, the 10-T OHC stores 16.6 GJ of energy when fully charged, and this translates to expensive electric power handling costs for the OH and hybrid burn cycles, as we shall see.

We next inquire regarding the impact of mechanical fatigue on the OHC performance. Below a stress cycle lifetime of $N_\sigma \approx 3 \times 10^4$ the steel bands are sized for a stress level of S_m = 500 MPa (the lesser of two-thirds the yield stress and one-third the ultimate stress for 316 LN at 4.2 K). Fatigue data for steel [6] indicate that the stress levels must be reduced to guarantee survival for a larger number of cycles. Since stress is reduced by increasing the thickness of the structural steel bands holding the OHC together, there are two detriments associated with an increasing N_σ. First, the OHC cost increases; and second, the solenoid winding increases in thickness, reducing R_{OH} and the flux $\phi_{OH,p}$. These trends are displayed in Fig. 11, using a safety factor of twenty on fatigue cycles. For $N \gtrsim 5 \times 10^5$, where the strain amplitude is $\varepsilon \lesssim 0.001$, the lifetime becomes insensitive to N_σ. For high cycle lifetimes the increase in OHC cost is substantial, ~50-70% more than the base cost. The decrease in transformer flux at high cycles (~7%) is not as significant for the 8-m reactor as it would be for a reactor with a smaller major radius operating in the OH cycle. We assume that any resistivity increase due to work hardening of the copper stabilizer can be removed by annealing during machine warm-up periods. We note that fatigue data for NbTi composite and multi-strand cable are unavailable, and additional unpleasant surprises could appear after long-term experience with highly pulsed coils.

4.2 Equilibrium Field Coils

Reference EFC configurations were developed for both the 8-m and 7-m reactors. The 8-m device imposes two constraints on the EFC system — the EFC should be decoupled from the OHC (zero mutual inductance), and EF coils are

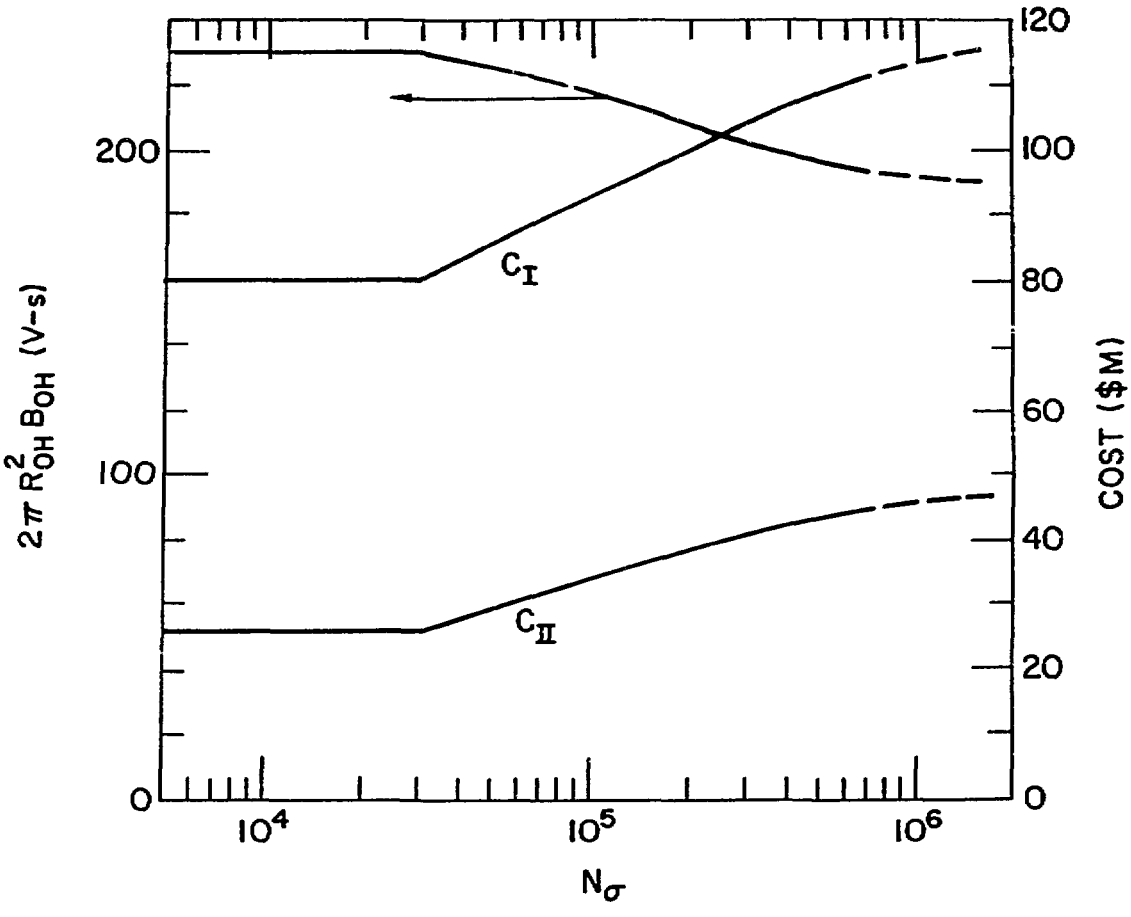

Fig. 11. Complete OHC winding cost ($1983) and approximate flux versus cyclic life; B_{OH} = 10.0 T, R_0 = 8.0 m, 316 LN structure.

restricted from the central hole, which is occupied by the OHC. This results in a system with substantial stored energy, U_{EF} = 6.36 GJ, a large coil volume, V_{EF} = 177 m^3, and relatively small coupling to the plasma, $\phi_{EF,p}$ = 71 V-s. On the other hand, burn cycles without an OHC offer relaxed constraints on the EFC design. For the 7-m reactor an attractive EFC system can be designed: U_{EF} = 5.61 GJ, V_{EF} = 136 m^3, and $\phi_{EF,p}$ = 95 V-s. Comparing the reference EFC systems for the 8-m reactor (with OHC) and the 7-m reactor (without OHC) we see quantitative advantages of the latter configuration, which are mainly due to the ability to locate an EF coil near the inboard midplane. These advantages are not large, however, since the 7-m reactor has the

higher plasma current (in order to achieve comparable performance with the 8-m reactor). The advantages of inboard coil placement are greatly magnified, though, if a more highly triangular ($d \gtrsim 0.5$) or "bean"-shaped equilibrium is desired. The strong increase of stored energy with triangularity is well known [25]. Thus the stored energy and EF power supply costs for the 8-m reactor in this study must be viewed in the perspective of the rather mild triangularity ($d = 0.2$) selected for the plasma equilibrium.

Next we evaluate the EFC cost and lifetime. As in the case of OHC, the cost of the conductor and structural materials for the EFC is estimated for a 50-kA cable design. The cable configuration is assumed to be helium-I (4.2 K) pool-boiling coils with niobium-titanium and copper stabilizer (same as the OHC outer ring coils). The cost of the EFC for the 8-m reactor is based on material requirements of 170 Mg of copper and 14.7 Mg of NbTi; in the absence of fatigue, 689 Mg of steel is needed to achieve stress levels of $S_m = 500$ MPa. Figure 12 shows the increase in EFC cost to accommodate increased

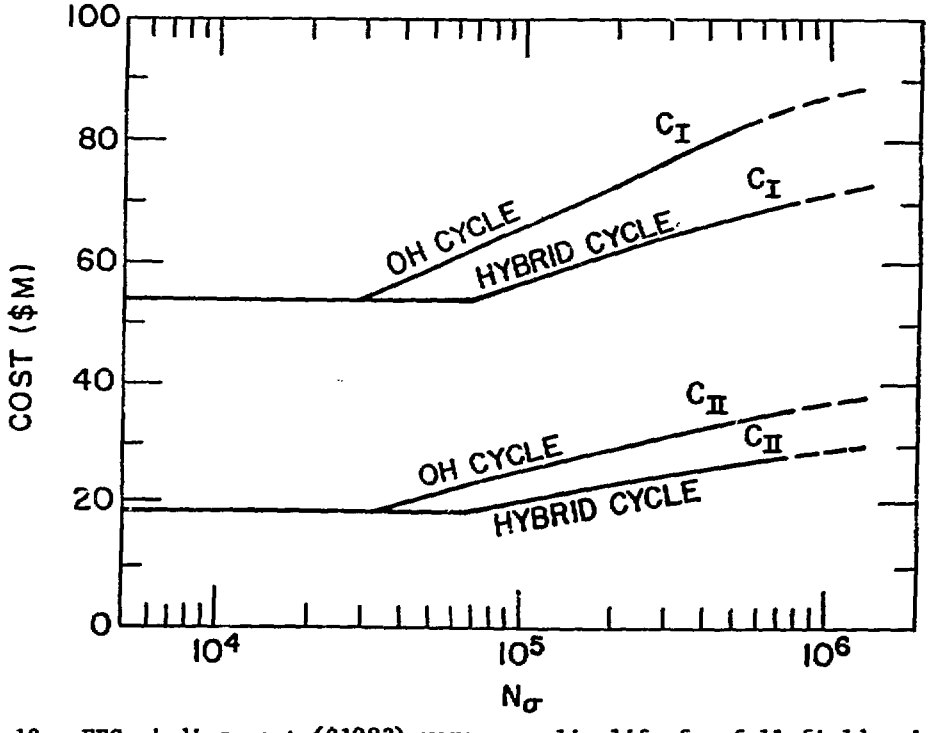

Fig. 12. EFC winding cost ($1983) versus cyclic life for full field swing (OH burn cycle) and half field swing (hybrid burn cycle); 8-m reactor, 316 LN structure.

mechanical fatigue at large N_σ. We recall that hybrid burn cycle reduces the vertical field B_{EF} to about one-half the full field value, so stress variations are only approximately three-fourths of the variation experienced with the conventional OH cycle. This accounts for the less expensive structure and overall cost displayed in the figure. Finally, we note that the IT burn cycle may require a still more expensive EFC since B_{EF} must increase during the overdrive phase above the values required for OH operation.

4.3 Toroidal Field Coils

For the purposes of our burn cycle study we use a simple constant-tension D-shaped TF coil model [26]. The results, in Table 3, show the winding costs to be similar for both the 7- and 8-m reactors.

TABLE 3

Reference TFC Systems

Parameter	8-m reactor	7-m reactor
Maximum field, B_M	9.81 T	11.2 T
Inboard leg, R_1	4.06 m	3.19 m
Outboard leg, R_2	14.15 m	13.02 m
Number of coils, N_{TFC}	12	12
Full perimeter, L	39.0 m	39.3 m
NbTi mass, m_{NbTi}	54.6 Mg	45.6 Mg
Nb_3Sn mass, m_{NbSn}	1.78 Mg	4.60 Mg
Copper mass, m_{Cu}	2122 Mg	2130 Mg
Co-wound steel, m_{SS}	1717 Mg	1660 Mg
Winding cost, long-term, C_{II}	$109.9 M	$107.3 M
Radial build (helium vessel), Δ_{TFC}	0.75 m	0.94 m
Coil width (helium vessel)	2.13 m	1.67 m
Helium vessel thickness, t_{He}	4.0 cm	4.0 cm
Unsupported length	11.85 m	11.39 m
Maximum bending moment, M_{max}	131 MN-m	103 MN-m
Shear panel, height × width	9.61 × 4.00 m	9.63 × 4.03 m
Force on shear panel	62.1 MN	79.8 MN

Designs based on co-wound steel structure at 550 MPa; constant tension shape; 1983 dollars.

The principal burn cycle related differences in TFC designs arise from out-of-plane forces generated by OHC and EFC current variations. The thickness, t_v, of the steel vacuum dewar which surrounds the helium vessel is a variable in our study which is adjusted to provide adequate stiffness of the unsupported span of the TFC against fatigue failure. Likewise, the thickness of the shear panel, t_s, is selected to provide fail-safe resistance to the overturning torque on the TF coils.

In order to select the required thickness of the vacuum tank to limit the fiber stress on the side wall, a crack propagation analysis of the steel case is undertaken. Standard fracture mechanics [27] methods are used to predict the crack width, a, as a function of the number of stress cycles N_σ. The variable stress intensity is proportional to the maximum stress during the cycle and to the square root of the crack size, $\Delta K = 1.2\ F\sigma_M\sqrt{\pi a}$. The factor F depends on how the stress variation compares to the maximum stress. For example, fully cyclic stress, from $+\sigma_M$ (tension) to an equal but opposite stress, $-\sigma_M$ (compression), is more damaging than cycling between σ_M and zero stress. We use the damage model which characterizes most metals [22], $F = (1 - R_s)^{0.6}$, with $R_s \equiv \sigma_m/\sigma_M$, σ_m being the minimum stress. Figure 13 displays the maximum permissible stress for a given number of cycles to failure for various initial cracks, a_0, assuming safety factors of two on stress and four cycles, for room temperature annealed 316 LN [6]. We see that, for typical a_0, tens of thousands of cycles to failure occur for $\sigma_M \approx 200$ MPa. Generally, higher σ_M is permissible if a smaller number of cycles is specified. In any event, the stress should not exceed S_m, which is 217 MPa at this temperature. Thus, there are no significant reductions in structural requirements for the TFC once the total number of vertical field cycles is reduced below about ten thousand.

The stress variations are quite different among the tokamak burn cycles we consider. For the hybrid and internal transformer modes B_{EF} typically cycles between full and half-field values, so $R_s = 0.5$ and the bottommost abscissa can be used. Note that each stress cycle corresponds to one fusion burn cycle in this case. In the single swing OH burn cycle the OHC is reset to the same polarity before each burn, so the plasma current always flows in the same sense, the out-of-plane force is always in the same direction and $R_s = 0$. The figure shows, from the middle abscissa, that fewer cycles to failure

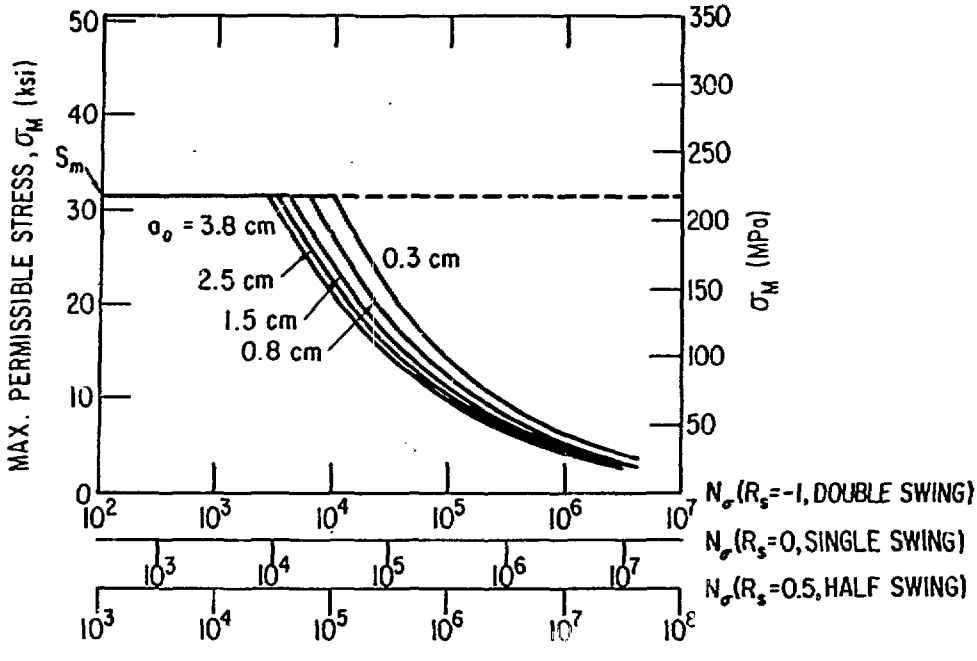

Fig. 13. Fracture mechanics limited stress, 316 LN (annealed) at 293°K.

can be tolerated under these conditions compared to the half swing. The worst situation obtains if B_{OH} swings both directions, reversing toroidal current and OHC polarity on alternating fusion periods. Then $R_s = -1$, and even fewer stress cycles are tolerable than for single swing operation of the EFC. Note, however, in this mode two fusion burn periods occur for each mechanical stress period.

Controversy exists over what initial crack sizes should be considered for failure analysis. Conservatism dictates the choice of relatively large a_0, since inspection of the fabricated steel structure becomes expensive and unreliable for small flaws. Moreover, the failure to detect an initial crack could have serious consequences; even though TFC monitoring is advisable, periodic remote inspection will prove challenging, and replacement of a weakened TFC with a growing crack may prove impractical. On the other hand, inspection techniques may not differentiate between harmless stress risers of dimensions a_0 (for example, bubbles) and true cracks. In this case fracture

mechanics could severely underestimate the cycle lifetime of the steel structure. With these caveats in mind we proceed to use fracture mechanics with initial crack lengths assumed to be one-tenth the thickness of the vacuum tank, $a_0 = 0.1 \times t_v$.

The free span of the TFC is treated as a straight, rigid nested box beam. The moment of inertia of the helium vessel, I_{He}, is found and that of the vacuum tank, I_v, is found for various tank wall thicknesses. The total moment, $I_{He} + I_v$, is used to infer the fusion cycle lifetime; from the dewar thickness, t_v, the volume of steel (hundreds of cubic meters) and cost of the vacuum tank are determined. In our analysis we take the beam to be simply supported at both ends. (This treatment yields close agreement of maximum bending moment and out-of-plane deflection when tested against the finite element analysis of Ref. 6.)

The cost of the vacuum tank, based on \$24/kg (the estimated cost [6] in 1983 dollars) is shown in Fig. 14. As expected, the cost is level up to $N_f \sim 10^4$. Hence, a reactor with a day-long burn ($t_f \sim 10^5$ s) has a vacuum tank no more expensive than that of a CW reactor ($N_f \sim 200$, $t_f \sim 3$ mo). However, shorter burns accumulate fatigue damage very quickly. For short burns ($t_f \sim 10^3$ s, $N_f \sim 10^6$) the incremental structural costs become prohibitive. We caution, though, that our cost estimates may be too high at large N_f. At tank costs of \$100 M to \$200 M the steel side walls are in the range of 20-cm to 30-cm thickness. It may prove impractical to form such large, thick members. The prohibitive costs at this point would drive us to consider alternative structural support. For example, an intercoil support structure might be used in order to drastically shorten the unsupported free spans of the TFC, perhaps reducing costs by large amounts. So we must conclude that the particular model (patterned after STARFIRE) used in our present study may become inappropriate for TFC structure experiencing millions of lifetime cycles.

We note that there are large differences among the burn cycles for a fixed N_f. The double-swing OH cycle has the largest stress fluctuations and hence requires the most massive structural support. For the same N_f a single swing OH cycle results in cost savings. Even more attractive is the hybrid burn cycle, since the stress fluctuation is so modest ($R_s = 0.5$). For IT operation the relatively small stress fluctuations are overshadowed by the much larger number of pulses envisioned for the life of the reactor ($N_f \gtrsim 10^6$),

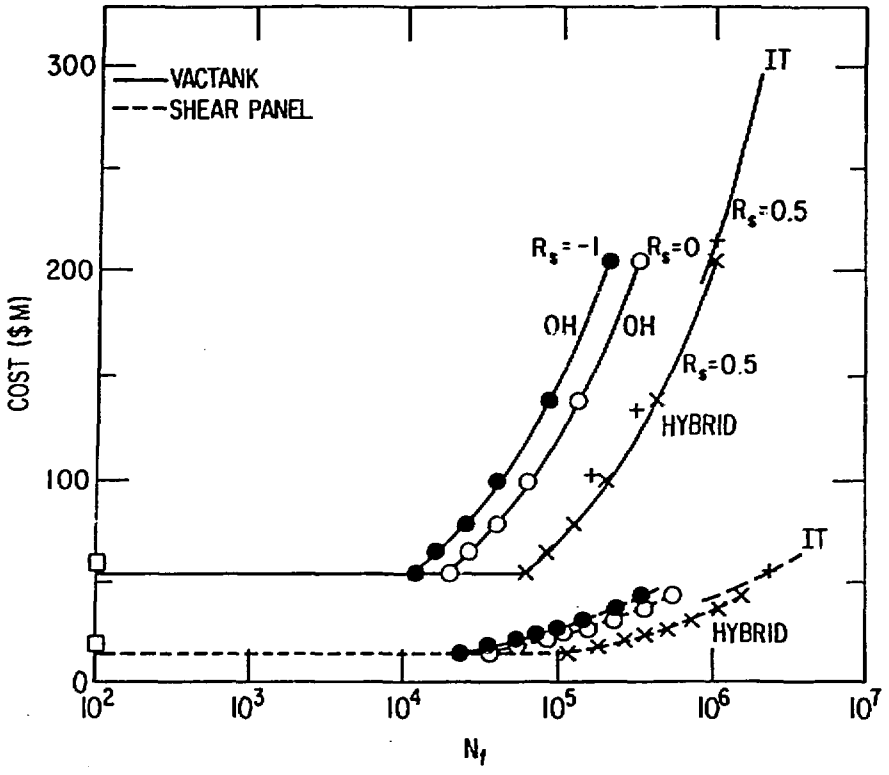

Fig. 14. Structure cost for TFC vacuum cases and shear panels. Box indicates CW, 7-m reactor.

with the net result that this cycle is likely to be the least attractive in terms of TFC structural costs.

As with the vacuum tank a fracture mechanics life analysis can be performed for the shear panels. The cost of the shear panels for various burn cycles is also shown in Fig. 14. The cost trends exactly parallel those for the vacuum tank, but their magnitude is considerably smaller.

We see that a single swing OH cycle operating with a one-hour burn ($N_f \sim 3 \times 10^5$) will entail capital costs at least \$100 M higher than a reactor operating in the CW mode. This disparity is greatly reduced if the ohmic burn period can be extended to 8 h or more. If neither of these options is available but a hybrid burn cycle is used, then any fusion cycle period exceeding about 30 min becomes competitive. The internal transformer cycle seems unattractive since it has such a tremendously large total number of cycles in the reactor lifetime ($N_f \gtrsim 10^6$). A completely different design philosophy would be required to accommodate coil fatigue in such a case.

Last, we address the problem of eddy current heating in the TFC system. The dominant heat source is due to poloidal field component variations normal to the cryogenic steel structure encasing the winding, the 4-cm thick helium vessel. Following the method of Ref. 28 we find that the heating per length along the TFC helium vessel is $dP/d\ell = I_{He}(\dot{B}_{\perp})^2/\rho$, where I_{He} is the out-of-plane bending moment of inertia, and where ρ is the case resistivity. We find numerically that the electric refrigeration power is nearly always negligible in the reactor's power balance. Likewise, capital cost for refrigeration is quite small compared to the overall power plant cost. We thus conclude that burn cycle alternatives have a relatively small impact on the reactor cost and performance from considerations of eddy current heating.

4.4 Blanket Thermal Effects and Thermal Energy Storage

Of two viable breeding blankets studied, one with a solid breeder and water coolant and one with self-cooled liquid lithium, only the former is investigated with a detailed burn cycle analysis [6]. We consider a model burn cycle with a 1-h burn, 10-s linear power decrease, and a variable dwell period, t_{dw}, followed by a 10-s power increase. Explicit blanket temperature variations are calculated for four cases: t_{dw} = 0, 30, 90, 200 s. During the burn the wall load is set at W_n = 3.45 MW/m^2.

The solid breeder blanket contains Li_2O granules and is punctuated by ten rows of cooling tubes designed to maintain (steady-state) temperatures between 410°C and 800°C in the breeder. Coolant inlet/outlet temperature is 280°C/320°C. Experience shows that an acceptable assessment of this system can be carried out with results based on only three representative blanket regions. We calculate the transient temperature response near the first wall (100% of the nuclear power density, 41 W/cm^3), at the 25% power region, and at the back of the blanket (5% power). Since the volume of the blanket region associated with each coolant channel in an exponentially decreasing nuclear power field increases as the blanket regions are located further away from the first wall, the thermal inertia of regions in the radial direction (depthwise) increases. Our results agree rather well with a simple model proposed by Deis [29]. As expected, the changes in the coolant outlet temperatures and temperature gradients in the Li_2O blanket increase as the dwell times increase. If the dwell times are sufficiently long ($\gtrsim$ 200 s), the temperatures of components are found to decrease to the coolant inlet values.

Thermomechanical fatigue may not be critical to the porous Li_2O mass, which is fabricated at only 85% of theoretical density. Cooldown of the breeder below its lower operating limit can affect tritium recovery, but this may be unimportant if the duty factor is high. Thermal stresses across the coolant tubes during power transients (<5 MPa) are much less than the primary stress (~55 MPa) due to the high pressure coolant (at 15 MPa) so fatigue is insignificant. Dimensional changes are possible at the breeder/cooling tube interface after cyclic operation. Although this could adversely affect the thermal conductance at the interface it might be controlled with a metal felt sleeve around the tube. In all, no severe degradation of the blanket life is anticipated due to cyclic operation.

Although, due to their lower thermal inertia, the high power blanket regions have faster time response and larger temperature fluctuations than the low power regions, these differences are averaged as the water flows from the cooling tubes and is mixed in the headers leading to the steam generators. Figure 15 displays the mixed coolant temperature for one case, t_{dw} = 30 s. Note the temperature drops steadily for 40 s to 304°C but requires several minutes to recover once nuclear heating returns. Even for t_{dw} = 0 s (10-s power drop followed by an immediate power ramp), the limiting case for IT operation, the coolant drops to 313°C. Since the electric power is proportional to coolant temperature rise in the blanket, we find the generator output drops transiently to (313-280)/(320-280) = 83% of its steady state rating even with this shortest dwell. Moreover, the whole power conversion system [1] is based on coolant outlet temperatures of 320°C which generate slightly saturated steam (299°C at 6.3 MPa), so coolant temperatures below ~300°C result in wet steam at 279°C entering the turbine. Both steam temperature fluctuations and moisture content are damaging to the turbine blades, but this may not be critical if the burn cycle's duty factor is very high. We assume the dominant concern is the transient electric output of the fusion power plant. Hence, we must provide an energy storage system which supplies the whole energy deficit during the dwell with a fast time response to keep the electric power constant.

For a 4000-MW thermal reactor, the energy deficit varies from 40 GJ to over 800 GJ as t_{dw} varies from 0 s to 200 s. Several thermal storage systems, such as packed columns of metals or ceramics, and chemicals, were considered

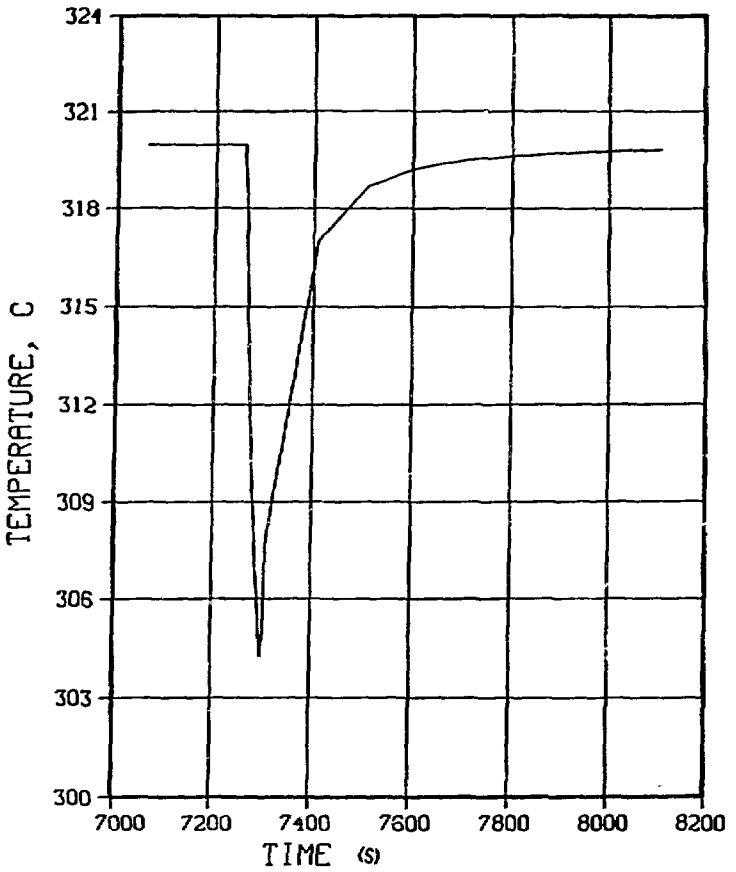

Fig. 15. Volumetric average temperature response: 30-s dwell.

for energy storage. However, they did not appear to be practical if the thermal energy is to be withdrawn in a relatively short period of time. Energy storage in pressurized water, which can be withdrawn as steam by flashing [30], or energy storage in a high temperature liquid metal which can be fed into a heat exchanger/evaporator unit appear to be practical, although such systems are considered to be at the upper end of existing technology. Analyses show that a pressurized water/steam system is suitable for the solid breeder blanket, and a hot sodium reservoir would be practical for the liquid lithium blanket. A detailed description of the two systems is available in Ref. 6, and the component costs are summarized in Tables 4 and 5.

TABLE 4

Cost of Thermal Storage System:* Water-Cooled Li_2O Breeder

	Basic cost	Cost of additional components for 10-s dwell
High pressure vessels (@ $14 M each)	28	28
Charging pumps	10	
Piping	5	1
Valves	8	
Condensate storage	5	1
Instrumentation and control	5	1
Building and structures (incremental)	4	2
Installation	8	4
Total	71	37

*$M (1983).

TABLE 5

Cost of Thermal Storage System:* Self-Cooled Lithium Blanket

	Basic unit	Cost of additional components for 10-s dwell
Storage vessels	6.5	6.5
Sodium charge	0.3	0.3
Piping	3.6	1.8
Valves	7.1	4.0
Building and structures (incremental)	2.6	1.5
Gas blanket and emergency venting	1.2	0.6
Sodium cleanup system	2.0	0.6
Instrumentation controls	3.0	1.2
Installation	4.0	1.5
Miscellaneous	2.0	1.0
Total	32.3	19.0

*$M (1983).

In comparing burn cycles we base thermal storage costs on the results in the tables; for the water/steam and lithium/sodium/steam systems we have respectively

$$C_{H_2O} = \$71\ M + [\$3.7\ M \times t_{dw}(s)]$$

$$C_{Na} = \$32\ M + [\$1.9\ M \times t_{dw}(s)] .$$

Examination of the cost of thermal storage for the two systems indicates that the costs for the liquid-lithium breeder is significantly lower. The primary reason for the low cost of the liquid-metal system is due to low-pressure operation of the thermal storage system (1.5 MPa liquid-metal breeder versus 15 MPa for water-cooled solid breeder). It should be noted, however, that the liquid lithium blanket was studied in less detail; the added cost of tritium containment such as double-wall pipes, penalty for heat exchangers due to added thermal resistance of double-wall pipes, tritium cleanup, and recovery systems have not been included in this analysis. Although thermal energy storage is rather cheap ($\sim\$1.0 \times 10^{-3} - \$5.0 \times 10^{-4}$ per joule) compared to electric energy storage, it appears to be a major cost item for pulsed burn cycles due to the tremendous energy storage required for long dwells.

4.5 Auxiliary Power for Heating and Noninductive Current Drive

Dynamic simulations of reactor startup suggest 75 MW of plasma heating for $t_{EF} \sim 5$–10 s is adequate for ignition. We assume the same power source (ECRH, ICRH, etc.) can be used for both heating and current drive, and, thus, we assign a cost penalty for noninductive current drive only for that portion of absorbed power which exceeds 75 MW.

The capital cost for high power rf equipment is difficult to estimate, for several reasons. First, CW power systems exceeding 100 MW have not been built, so learning curves and economies of scale are hard to predict. Also, some technologies (ECRH) are not advanced to the point that high power CW sources are available. Likewise, system costs are sensitive to requirements such as mode purity, tunability, bandwidth, launcher design, radiation and electrical protection, and transmission efficiency. In Fig. 16 we display curves of estimated capital cost versus power launched into the tokamak, for

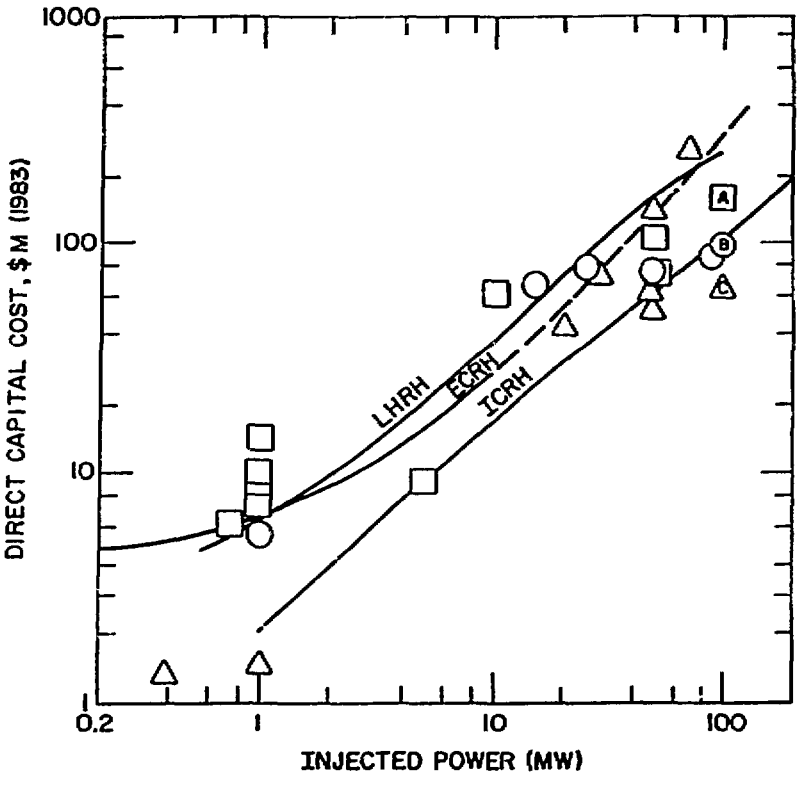

Fig. 16. RF capital cost modeling and data. Specific designs are denoted by boxes for ECRH, circles for LHRH, and triangles for ICRH; point A is from Ref. 16 and B and C are from Ref. 17.

three frequency regimes. The isolated points represent existing or near-term systems at the 1-MW level and published fusion designs (see, e.g., Refs. 31 and 32) at the 100-MW level; the scatter among the points indicates our level of uncertainty in cost estimates.

Regarding the overall power transfer efficiency, η_d, of rf systems we find from a literature survey that the ac-to-rf efficiency could vary from a low of ~23% for ECRH to a high of ~55% for LHRH and ICRH. This relatively low η_d figures prominantly in the economics of the CW burn cycle.

4.6 Electric Power Supplies and Energy Storage

The type and cost of electrical components for a tokamak depend on details of the burn cycle. In particular, power supply costs generally decrease as the time between burns increases since the magnets can be energized over

longer periods. Countering this is the trend to more expensive thermal storage as the dwell period increases. In this section we explore this tradeoff to identify the optimum operating parameters for each burn cycle, including the cost of a noninductive current drive system when applicable.

The double-swing OH burn cycle is studied first. Based on a detailed analysis of the burn cycle of the 8-m reactor with a profile-averaged time-dependent plasma code, general features and operating algorithms were developed for use in the parametric burn cycle study. Additional insight to the power supply aspects of tokamaks is available in Ref. 33.

The circuit diagram for the OH cycle is shown in Fig. 17. As shown in the figure the OHC is driven by two types of energy transfer devices. A dump resistor/SCR switch system is used for startup to ramp down the initially charged OHC in the Ohmic heating time, t_{Oh}. This resistor could probably be of the nonlinear type, e.g. zinc oxide, or silicon carbide as proposed for the TFTR- OH system [34]. The resistor is modeled as having an ideal, i.e. constant, voltage drop, when connected. The same resistor is also used for the shutdown. During the burn period the OH current is slowly ramped up to make up for resistive losses in the plasma. The power needed to do this is relatively small, ~15 MVA. Finally, after shutdown, the OH coil must be recocked to the full 10-T value for the next burn pulse. This is done in the dwell period, t_{dw}. During the dwell period the plasma chamber is evacuated and then filled with fresh deuterium-tritium gas for the next burn pulse. The recocking OH power supply is a rectifier/invertor SCR-type supply operating out of an MGF set. The cheapest way to recock the coil, which stores ~17 GJ at full field, is to alternate the direction of induced plasma current every pulse. We recall however, that this double-swing current mode aggravates the toroidal magnet fatigue; thus, the power supply cost saving might be offset by the need for a more expensive TFC system. Another cost saving technique is to use the same OH recocking SCR supply to drive the EF coil during startup and shutdown and the OH coil during the burn phase. The SCR power supply requirements are then set by whichever system, EF or OH, has the maximum power needs. A low density startup, together with initial rf heating, is used to minimize resistive volt-second losses. Thus the plasma is kept fairly hot throughout the Ohmic heating portion of the cycle. The resistive volt-second loss during startup is typically 5 V-s.

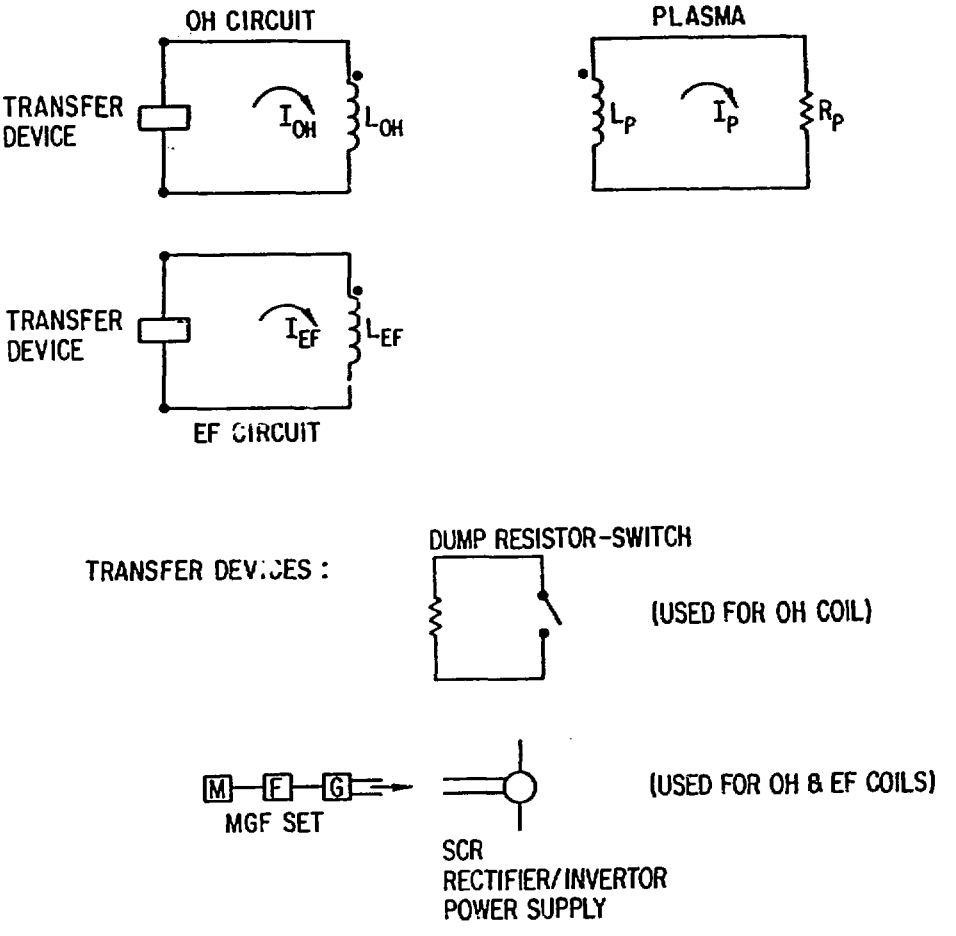

Fig. 17. Power supply system for a conventional OH cycle. Cycles with noninductive current drive have an additional (rf) current source in the plasma circuit and have no dump resistor; moreover, the IT and CW cycles have no OH circuit.

The second phase of the startup is defined as the EF ramp. During this period the plasma is heated to ignition and the EF current is brought to its full value. Throughout the startup the EF current is raised to maintain the plasma in MHD equilibrium. The EF power requirement is given by the product of the maximum EF voltage and the maximum current. In order to minimize the EF voltage during startup, the rf heating is modulated to maintain a fixed rate of net heating power during different portions of the cycle. In addition, xenon is added towards the end of the startup to establish plasma thermal stability.

For the 8-m reactor a burn time of ~51 min can be obtained, based on the OH flux swing of 307 V-s available for the burn period and assuming a plasma loop voltage of ~0.10 V (Spitzer resistivity with an anomaly factor of 2.5 due to, e.g., trapped electrons).

We find the following approximate formulas describe the energy transfer system (ETS) requirements in general:

$$P_{OH} = \frac{\Delta\phi_{dump} \times I_{OH}^{max}}{t_{OH}}$$

$$P_{OH}^{*} = \frac{0.75\ \Delta\phi_{dump} \times I_{OH}^{max}}{t_{dw}}$$

$$P_{EF} = \frac{U_{EF}}{t_{EF}}$$

$$P_{max} = \max\left(P_{OH}^{*},\ P_{EF}\right) ,$$

where P_{OH} is the reactive power isolation requirement of the dump resistor/-switch, P_{OH}^{*} is the OH recocking requirement, P_{EF} is the EF reactive power requirement (for $t_{EF} \lesssim t_{OH}$), and P_{max} is the reactive power requirement of the SCR supply used for both OH recocking and EF drive. P_{max} is also the requirement of the generator portion of the MGF set. The other parameters are $I_{OH}^{max} = 163 \times 10^{6}$ A, $\Delta\phi_{dump} = 163$ V-s, and $U_{EF} = 6.36$ GJ. The stored energy requirement of the MGF set is approximately constant, at ~30 GJ. Finally, the thermal storage system time requirement is given by:

$$t_{down} = 2\ t_{OH} + t_{EF} + t_{dw} .$$

This downtime is the time over one burn cycle when no fusion power is produced, considering the fact that there is some fusion power during the EF ramp-up and ramp-down periods.

The power supply cost algorithms [33], based in part on TFTR experience, are (in 1983 dollars):

$$C_{OH} = \frac{\$0.016}{W} \times P_{OH} .$$

$$C_{max} = C_{SCR} + C_{MGF} = \frac{\$0.1}{W} \times P_{max} + \$70\ M\ ,$$

where C_{OH} is the cost of the dump resistor/switch and C_{max} is the combined cost of the SCR supply and the MGF set. The thermal storage cost is a generalization of our previous result, $C_{ST} = C_{H_2O}$ or $C_{ST} = C_{Na}$, where t_{dw} in Sec. 4.4 is replaced by $(t_{down} - 10\ s)$. The total ETS cost is thus: $C_{ETS} = C_{OH} + C_{max} + C_{ST}$.

A wide range of OH burn cycle parameters was examined. It was found that a choice of $t_{OH} = t_{EF}$ is about optimum for a fixed value of t_{dw}. The resulting ETS cost for this parameterization is shown in Fig. 18 for the H_2O thermal storage system. The results show graphically the tradeoff between the power supply and thermal storage costs. At short dwell times, $\lesssim$10 s, the recocking supply requirements become very high and dominate the cost. At longer times the increase in thermal storage cost offsets any savings in the power supply. For a given value of t_{OH} there is a broad minimum in cost for a 20- to 30-s dwell time. For the values of $t_{OH} = t_{EF} = 10$ s and $t_{dw} = 20$ s the ETS cost is ~430 M$ for the H_2O system. Thus the ETS cost is a substantial fraction of the total reactor capital cost.

Similar curves are obtained if the lithium/sodium thermal storage system is chosen [6], except all costs are ~$100 M less than those in Fig. 18. The best result in this case has $C_{ETS} = \$309$ M with $t_{OH} = t_{EF} = 10$ s and $t_{dw} = 30$ s. Hence we conclude that the advanced technology of liquid-metal thermal storage may result in substantial cost savings if a tokamak reactor must operate in a cyclic manner.

We consider next the hybrid cycle, which uses an OH coil to maintain plasma current during the burn and a noninductive current driver to maintain current during a period of time when the OHC is recocked. Similar types of power supplies are needed for the hybrid cycle as the conventional system except that an OH dump resistor is not needed. The toroidal current, I, is related to the noninductive current component, I_d, and the OHC current, I_{OH}, and EFC current, I_{EF}, by the following equations:

$$V_{OH} = L_{OH}\dot{I}_{OH} - M_{OH,p}\dot{I}$$

$$I = I_d + (-L\dot{I} + M_{OH,p}\dot{I}_{OH} + M_{EF,p}\dot{I}_{EF})/R\ ,$$

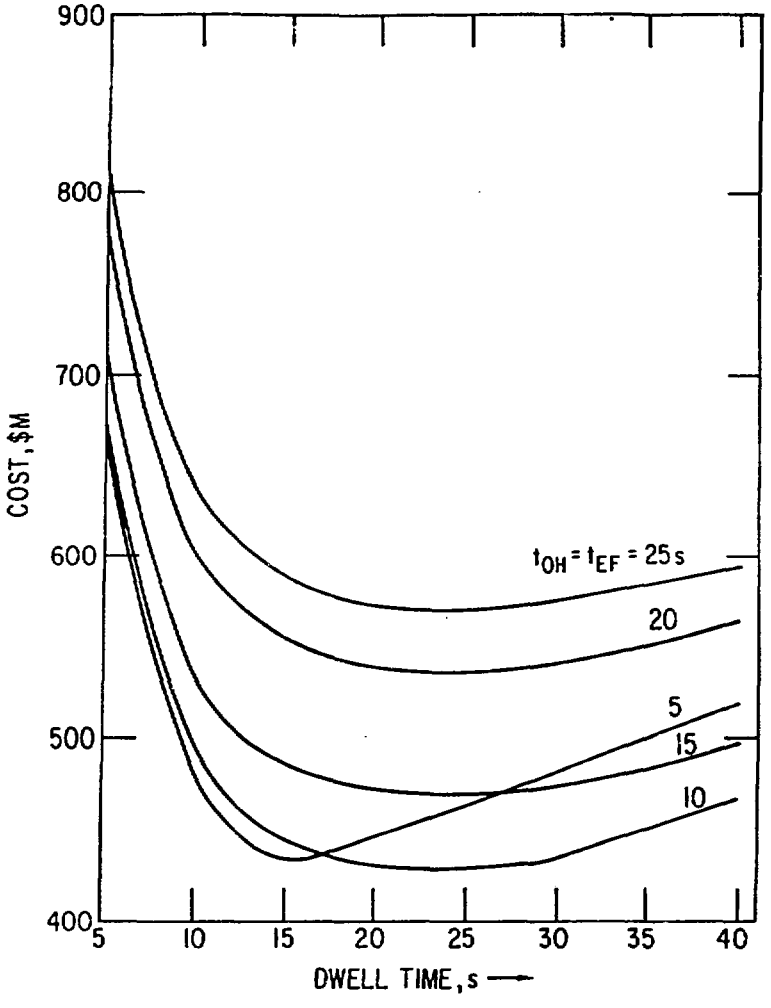

Fig. 18. Energy transfer system cost for a conventional OH double-swing cycle as a function of cycle parameters for a water thermal storage system.

where the M's denote the respective mutual inductances and with the toroidal self-inductance constant. During the OH recocking phase $\dot{I} = 0$ and $\dot{I}_{EF} = 0$. The required value of voltage needed to recock the OHC in the dwell time period is then given by:

$$V_{OH} = \frac{\Delta\phi_{OH,P}}{t_{dw}},$$

and the OH power required for recocking is

$$P_{OH} = \frac{4\,U_{OH}}{t_{dw}} .$$

The required value of I_d needed to maintain a constant toroidal current during the recocking phase is

$$I_d = I - \frac{V_{OH}}{R} ,$$

where the relation $M_{OH,p} \approx L_{OH}$ has been used.

For illustration we consider high-speed current drive, which has a driver power requirement given by $P_d = I_d n_{20}'/\gamma$, where we assume the density n_{20}' during the recocking phase is much lower than during the burn. Combining the expressions above we get the driver power in terms of γ and the dwell period:

$$P_d = \frac{n_{20}'}{\gamma}\left(I + \frac{|\Delta\phi_{OH,p}|}{R\,t_{dw}}\right) .$$

Thus the driver power depends linearly on the density during the recocking phase and also depends strongly on the plasma resistance during this phase. Obtainable values for these parameters, as well as γ, are uncertain. A brief analysis with our dynamic plasma code suggests $n_{20}' = 0.02$ and $R = 100\ n\Omega \equiv R'$ seem plausible.

The value of I during the dwell period is lower than for the burn period. This is because the reduction in EF current, necessary because of the reduction in plasma β, during the density ramp-down phase, reduces I. Conversely when the density is ramped back up, I_{EF} increases and ramps I up to its full value. From our simulation results of the 8-m reactor the value of plasma current during recocking was found to be $I = 10\ MA \equiv I_0'$.

The hybrid cycle offers several options in regards to the OHC design. One option, to be discussed first, is to design an OHC to give the same burn time as a conventional cycle. Since the hybrid OHC is only used to supply burn volt-seconds the OHC field strength for this option would be lower than for the conventional cycle. An alternative option is to use a different value of field to obtain a different burn time.

The value of OH field needed to obtain a burn time the same as for the conventional cycle is B_{OH} = 6.53 T. This gives a flux swing capability of $\Delta\phi_{OH,p}$ = 300 V-s. The stored OH energy at full field is $(6.53/10.0)^2$ = 43% of that for the conventional OH cycle, a considerable cost saving.

With the above parameters the required rf power is:

$$P_d = 10 \text{ MW} + \frac{3.00 \times 10^9 \text{ J}}{t_{dw}},$$

where we have presently assumed $\gamma/n_{20}^{\prime}$ = 1.0. For a value t_{dw} = 30 s, for example, P_d = 110 MW.

An additional cycle parameter is t_{EF}. The EFC reactive power is computed as for the OH cycle, and the thermal storage costs are calculated as before, except $t_{down} = t_{EF} + t_{dw}$. Finally, the incremental cost of driver power is taken to be C_d = (\$1.5/W)(P_d - 75 MW); this is the cost of auxiliary power above the 75 MW needed for ignition, assuming using a "typical" cost for rf systems (Fig. 16).

By varying t_{dw} and t_{EF} the total cost of the ETS can be calculated analogously to the OH burn cycle. Typical results are seen in Fig. 19, for $\gamma/n_{20}^{\prime}$ = 1.0, B_{OH} = 6.53 T, and water/steam thermal storage. The solid curves are C_{ETS} and the dashed cure is $C_{ETS} + C_d$. The dashed curve indicates that one would expect to pay a high price for recocking in short times, because of the high rf power needed. At long dwell times the costs go up due to increases in the thermal storage system cost. As with the OH cycle there is an optimum t_{dw} and t_{EF} which minimizes C_{ETS}; however, the cost of driver power tends to push the optimum t_{dw} to longer times than for the OH cycle. The best case (for $\gamma/n_{20}^{\prime}$ = 1.0, B_{OH} = 6.53) has t_{EF} = 13 s and t_{dw} = 45.8 s, resulting in $C_{ETS} + C_d$ = \$371 M. This is ~\$60 M less than the power supply cost for the OH cycle with the same burn length, which is due mainly to the elimination of the dump resistor and switch. As expected, considerable cost reductions are possible if the lithium/sodium thermal storage system is chosen; in the best case $C_{ETS} + C_d$ = \$256 M for $\gamma/n_{20}^{\prime}$ = 1.0 and B_{OH} = 6.53 T.

The cost variations for other values of $\gamma/n_{20}^{\prime}$ and B_{OH} are shown in Fig. 20. For the conventional and hybrid cycles the burn time B_{OH}, but t_f = 0 for B_{OH} = 4 T for the OH cycle since this is the minimum field needed to

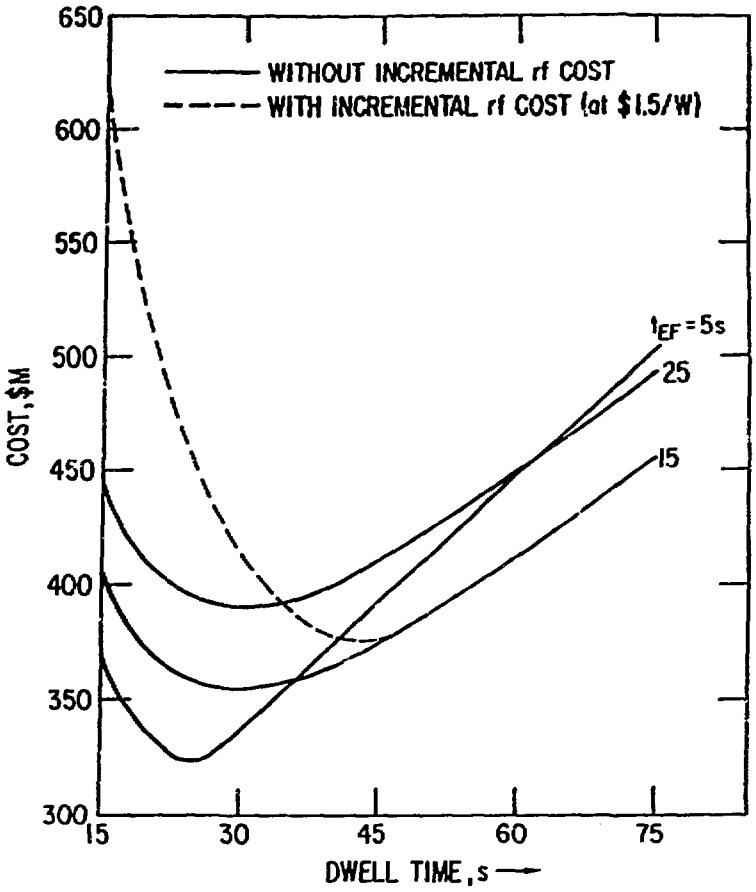

Fig. 19. Energy transfer system costs for a hybrid cycle, water system; B_{OH} = 6.53 T, γ/n_{20} = 1.0 A/W.

supply inductive volt-seconds for startup. We note for short burns ($t_f \lesssim 30$ min) that the hybrid cycle offers large cost savings relative to the OH cycle. At the other extreme we see the hybrid cycle offers the potential for longer burns than the conventional cycle, which could perhaps ameliorate some fatigue-related life limitations.

Turning to the IT cycle, we recall there is no OHC for this operating mode so the ETS consists only of the EFC power supply (SCR and MGF) and the thermal storage system. A fundamental parameter for the IT cycle is the plasma current overdrive ratio defined as:

$$\theta = I_1/I_0$$

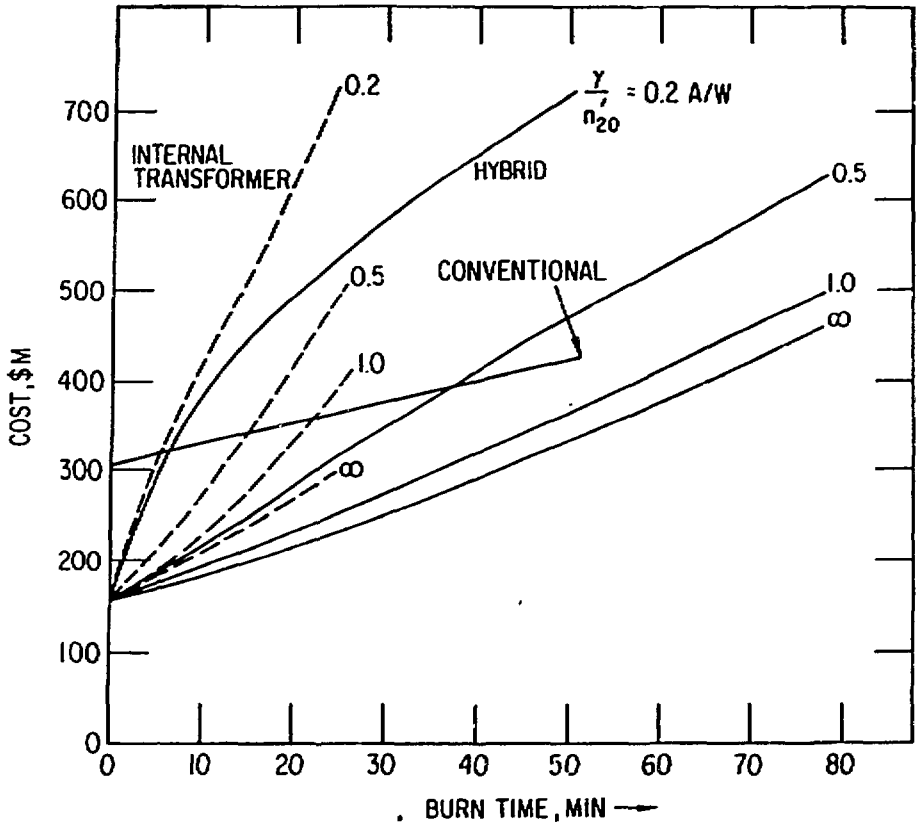

Fig. 20. Energy transfer system cost as a function of burn time and cycle type. [Includes incremental driver cost = \$1.5/W × $(P_d - 75\ MW)$ where applicable.] Burn time assumes 2.5 × Spitzer resistivity; all curves assume water/steam thermal storage.

where I_1 is the maximum plasma current used, $I_1 = I_0 + \Delta I$. For the IT cycle the plasma current is given by the current equations with $M_{OH,p} = 0$, and the burn time is $t_f = \Delta t_I = (L/R) \ln \theta$. During the current drive period the plasma current is given by:

$$I = I_d + (I_0' - I_d)e^{-t/(L/R')},$$

where L/R' is the plasma time constant during the current drive period and I_0' is the plasma current at the start of the current drive period. I_0' is some-

what less than I_0 due to the EF rampdown preceding the current drive period. We find that the dwell time necessary to obtain a current I_1 is given by:

$$t_{dw} = \frac{L}{R'} \ell n \left[\frac{1 - I_d/I_0'}{\theta - I_d/I_0'} \right] .$$

The EF ramp period for the IT cycle is similar to that for the hybrid. However, the EF stored energy is higher because of the higher plasma current. The EF power requirement scales approximately as:

$$P_{EF} = \frac{\theta^2 U_{EF_0}}{t_{EF}} ,$$

where U_{EF_0} is the EF energy corresponding to I_0. Neither the EFC design nor the plasma MHD equilibrium characteristics at higher values of plasma current were assessed for this study, but these may be serious issues for the IT cycle if θ is fairly large.

The final parameter for the IT cycle is the thermal storage requirement, given by $t_{down} = t_{dw} + t_{EF}$. The cost algorithms used previously can be applied to the IT system. Similar parameters to the hybrid cycle are used where applicable: $I_0 = 13$ MA, $I_0' = 10$ MA, $L/R' = 171$ s, and $L/R = 2236$ s.

The results of a parametric analysis of the IT cycle using a range of overdrive ratios from $\theta = 1$ to 2 are shown in Fig. 20. As shown, the IT cycle is limited to about one-half the OH cycle burn time, even with a (large) overdrive ratio of two. The cost of the ETS system depends on the current drive efficiency. However, for any given value of γ/n_{20}', the ETS cost for the IT cycle is always significantly more than the ETS cost for the hybrid cycle with the same burn length.

We close this section by remarking how the IT or hybrid cycle may offer cost reductions or possible extensions of t_f such as to reduce fusion fatigue cycles, N_f, relative to OH operation. Nevertheless, these cannot approach the promises of CW operation, for which we find $C_{ETS} \cong \$10$ M and $N_f \lesssim 200$. The relative attractiveness of CW versus pulsed operation depends partly on the cost, C_d, of the driver system, which we examine in the next section.

5. OVERALL BURN CYCLE COMPARISON: REACTOR DESIGN GOALS

For each burn cycle there are a number of factors (e.g., burn length, current drive efficiency) which we consider to be variable. A consistent comparison of burn cycles requires a simultaneous analysis of the various capital costs and cycle-related life limits as these parameters are varied. To this end we can isolate the several cost accounts of a tokamak reactor which are functions of the burn cycle parameters and monitor the total cost variation of the power plant.

Our costing is based on the STARFIRE accounting system [1], with all capital costs adjusted to 1983 dollars. The largest variable costs have already been discussed in Sec. 4. The power supply and electric energy storage systems are based on conventional technology, and we expect to see no significant reductions in unit costs beyond the values assumed. We find a factor of two difference in thermal storage costs and an even larger discrepancy in estimates of superconducting magnet costs. In order to bracket the level of uncertainty in our cost estimates we include both the high and low cost algorithms for thermal storage and magnet winding. (For all burn cycles the TFC winding is only costed with the STARFIRE method, C_{II}, however, in order that the CW reactor's direct cost be essentially the same as that of STARFIRE.) In addition to the magnet data in Figs. 11, 12, and 14, we find the helium vessel costs for the 8-m (pulsed) reactor OHC, EFC, and TFC to be, respectively, C_{OH}^{He} = \$3.1 M, C_{EF}^{He} = \$6.2 M, and C_{TF}^{He} = \$31.0 M; for the 7-m (CW) reactor these are C_{OH}^{He} = 0, C_{EF}^{He} = \$4.8 M, and C_{TF}^{He} = \$28.8 M. Our direct capital cost includes a 15% contingency allowance for all the variable cost accounts. For the reactors with noninductive current drive we include a cost, C_d, which accounts for the driver, and, based on Fig. 16, we illustrate this cost with two limits, \$1/W and \$2/W. Finally, the balance of plant (blanket, shield, heat transport, turbine, generator, buildings, etc.) is taken to be the same for all burn cycles, C_{BOP} = \$1736.9 M. (In fact, C_{BOP} should depend on factors such as reactor thermal power and gross electric power, as well as details such as neutron wall load and blanket/coolant type. All burn cycles have similar thermal power and wall loads, and, more importantly, we are only interested in the relative costs of the cycle-sensitive accounts. Hence a constant C_{BOP} is acceptable and mainly serves to place any cost variations in perspective to

the complete power plant capital cost.) In order to emphasize only the relative costs associated with different burn cycle choices, the summary illustrations, Figs. 21-25, display the total direct capital cost normalized to the STARFIRE value (1.00 ≡ $2062 M, total direct cost of STARFIRE in 1983 dollars).

5.1 Conventional (OH) Cycle

Capital cost and net electric power for the OH cycle are displayed in Fig. 21, assuming a 10-T external transformer is used with the 8-m reactor. The fusion period on the abscissa can be varied according to the achievable plasma resistance. The total cost varies mainly due to mechanical fatigue in the magnets and thus decreases for longer burns (smaller N_f). However, if longer t_f is achieved by geometry changes, for example larger major radius [15,17], we can imagine additional capital costs would be incurred.

Consider first double-swing operation. The upper curve in Fig. 21 is the cost estimate assuming water coolant/thermal storage and using the C_I formula for magnet winding cost and, hopefully, represents an upper limit on capital cost assuming relatively near-term technology. The lower curve includes liquid lithium/sodium coolant/thermal storage and the more optimistic C_{II} magnet cost algorithm and so predicts the best case, lowest costs typical of advanced technology and mass production manufacturing methods. For this operating mode the number of stress cycles, N_σ, for the TFC vacuum tank and shear panels is one-half the number of fusion (thermal fatigue) cycles, N_f; however, for the OHC and EFC, $N_\sigma = N_f$. We caution that our results for the TFC cost are unreliable for $N_f \gtrsim 2 \times 10^5$ since the two-way stress fatigue is so severe at this point that the STARFIRE TFC structure becomes unworkable. Note that the capital cost flattens out for $t_f \gtrsim 4 \times 10^4$ s ≈ 10 h. If $t_f \approx 16$ h is possible and the electric utility is willing to operate the fusion reactor as a peaking unit [17] (with diurnal electric power fluctuation) then an additional $200 M-$300 M could be saved by eliminating thermal storage and the MGF set. However, this would still be 15% more costly than the STARFIRE reactor, due to the OHC and its attendant electric power supplies.

For single-swing operation $N_\sigma = N_f$ for both the TFC and EFC; however, recocking the transformer for each burn now sets $N_\sigma = 2\ N_f$ for the OHC. The increase in power supply costs for this mode more than offsets any reductions

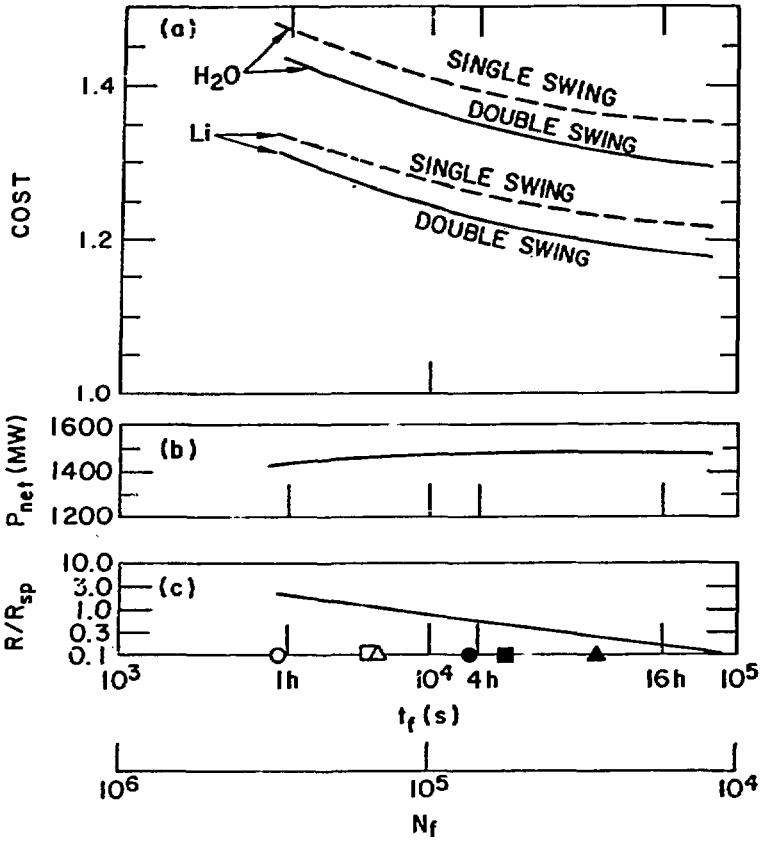

Fig. 21. OH cycle; B_{OH} = 10 T, 8-m reactor. (a) Upper cost curves represent water thermal storage and near-term magnet costs (C_I), and lower curves represent liquid sodium thermal storage and long-term magnet costs (C_{II}). Cost is total direct capital cost normalized to STARFIRE (Ref. 1) (b) Net electric power. (c) Plasma resistance required to obtain t_f, normalized to Spitzer resistivity, R_{sp}, with Z_{eff} = 1.70, $\bar{T}_e$ = 10 keV, and I_0 = 13.0 MA. Solid symbols are burn goals for worst case disruptions and thermal fatigue; open symbols are goals for moderate disruption damage (circles = limiter's leading edge, squares = limiter's front face, and triangles = first wall).

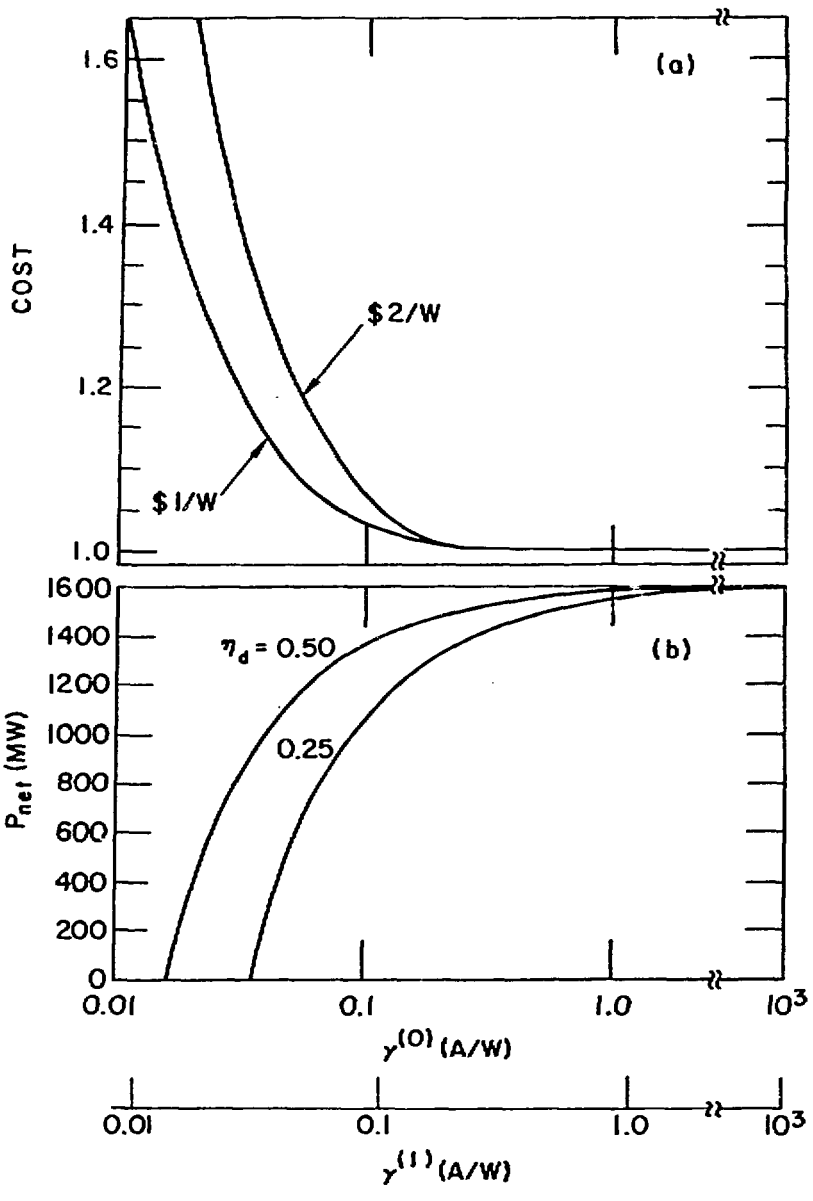

Fig. 22. CW cycle; 7-m reactor. (a) Direct capital cost for two values of current drive system cost; EFC winding costed with C_{II} formula. (b) Net power. Upper abscissa applies to high speed current driver, and lower applies to low speed driver. Note: $\bar{T}_e$ = 12 keV, n_{20} = 1.9, I_0 = 14.8 MA.

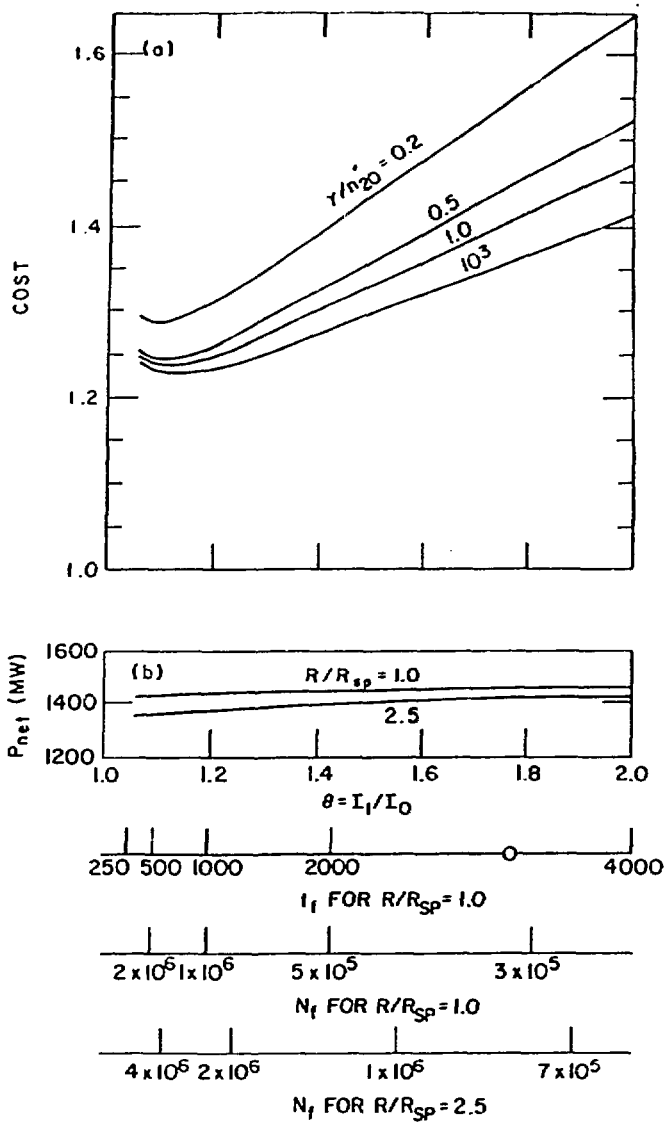

Fig. 23. IT cycle; 8-m reactor; $L/R' = 171$ s. (a) Direct capital cost based on water thermal storage and near-term magnet costs (C_I), with current drive system costed at \$1.5/W. Burn length and magnet fatigue based on $R = R_{sp}$. n'_{20} refers to the low density phase, and γ/n'_{20} is in units of A/W. (b) Net power, reflecting lower duty factor when $R > R_{sp}$; $\eta_d = 0.5$. Lowest abscissas denote lifetime cycles for given overdrive ratio, θ, but different plasma resistance R.

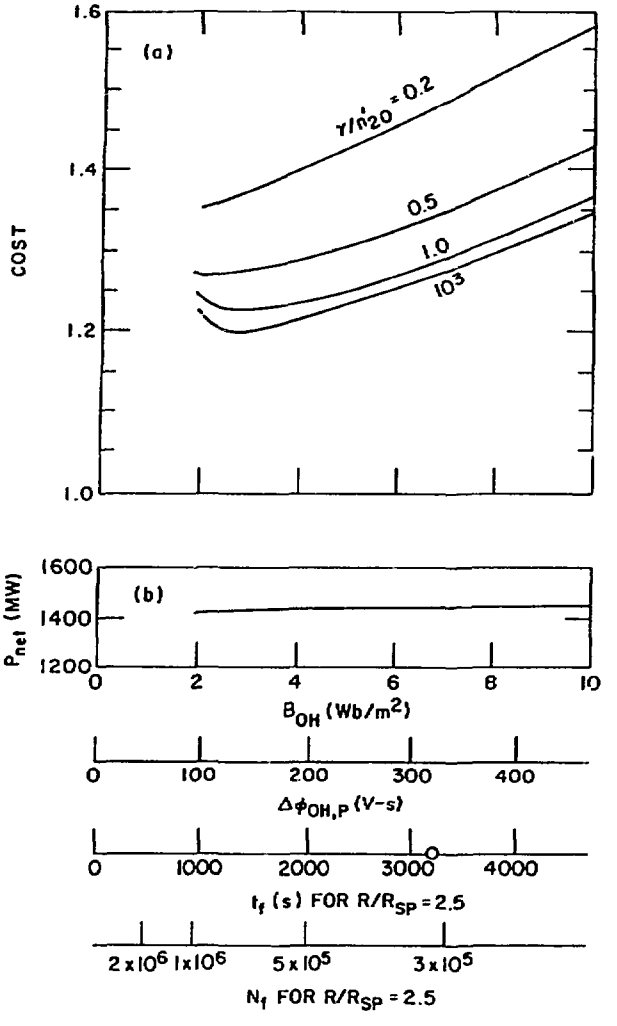

Fig. 24. Hybrid cycle; 8-m reactor, $L/R' = 171$ s, driver costed at \$1.5/W. (a) Direct capital cost based on water thermal storage, near-term magnet costs (C_I); and magnet fatigue with $R = 2.5\ R_{sp}$. (b) Net power. Top-most abscissa is full field in the OHC solenoid.

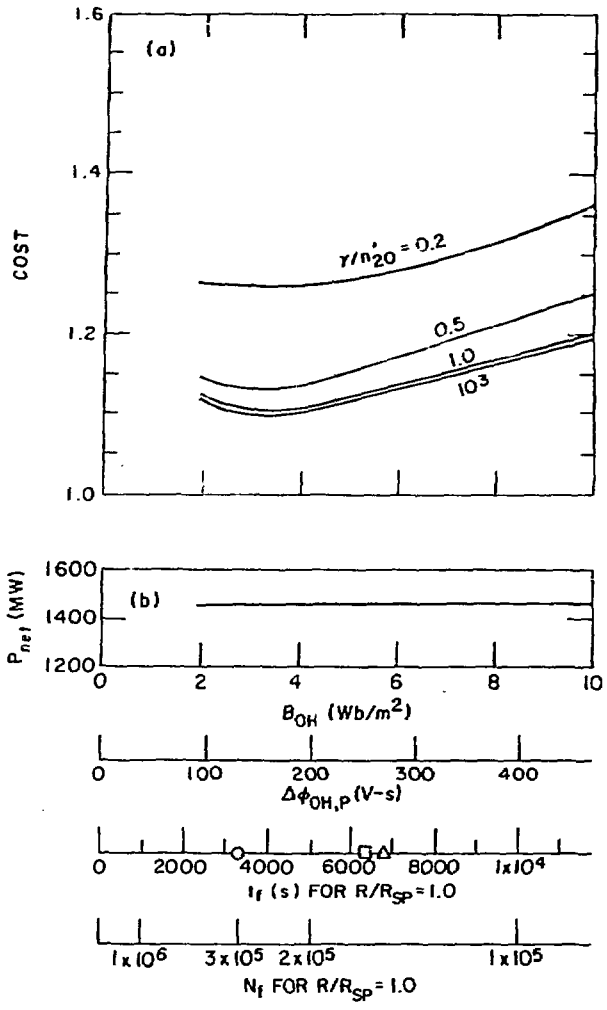

Fig. 25. Hybrid cycle: same as Fig. 24 except cost is based on sodium thermal storage, long-term magnet costs, and fatigue assuming $R = R_{sp}$.

in the TFC fatigue with the result that single-swing operation appears more expensive than double-swing operation.

For the OH cycle the duty factor is always large since $t_{down} \ll t_f$, so the net electric power, P_{net} exceeds 98% of the maximum possible for all t_f values plotted.

Besides reductions in capital cost at long burns ($t_f \gtrsim 10$ h), noted above, we recall that the first wall and limiter integrity are likely to improve with longer burns. Referring to Figs. 8-10 we find $t_f \gtrsim 3000$-7000 s is desirable in order to withstand moderate disruption damage at $W_n = 3.5$ MW/m^2. In the event of severe disruptions $t_f \gtrsim 1 \times 10^4 - 3 \times 10^4$ s is needed. We conclude that there are strong motivations for achieving t_f in excess of several hours for the OH burn cycle. However, for fixed reactor size ($R_0 = 8.0$ m) only modest extensions of t_f (beyond one hour) may be possible, for example, by reducing Z_{eff} or eliminating trapped electrons in order to lower the loop voltage.

5.2 Continuous (CW) Cycle

For very efficient current drive the CW cycle is exceptionally attractive since several complete subsystems (OHC, MGF, dump resistor, and thermal storage) are absent. The direct cost, as shown in Fig. 22, is much less than for the OH cycle in the high efficiency limit. The cost in the figure includes the noninductive current drive system, based on a price range of \$1-2/W, in accord with Fig. 16. Note that the required efficiencies for high speed and low speed current drive, $\gamma^{(0)}$ and $\gamma^{(1)}$, are nearly equal at $\bar{T}_e \approx 12$ keV. Comparing Figs. 21 and 22 we find the CW cycle becomes competitive in cost with OH operation once $\gamma^{(0)} \gtrsim 0.03$ A/W.

Of course, circulating power is a major concern for CW operation. At $\gamma^{(0)} \approx 0.03$ we see P_{net} is very sensitive to the current driver system efficiency. In fact, for the most credible range of $\eta_d \approx 0.25$-0.50 we project a need for $\gamma^{(0)} \gtrsim 0.07$ A/W in order to make the CW cycle appear reasonable. Thus, roughly a four-fold improvement in $\gamma^{(0)}$ is needed over the current experimental results [11,12]. A breakthrough in driver technology could relax this $\gamma^{(0)}$ requirement somewhat; for example, $\gamma^{(0)} \gtrsim 0.04$ A/W is probably acceptable if $\eta_d \approx 0.70$. Driver cost reductions (below \$1/W) apparently are not as important for a CW reactor as are improvements in η_d (above 0.50). In the other limit of large $\gamma^{(0)}$ or $\gamma^{(1)}$ we note that the best theoretical values (~0.2 A/W and ~0.16 A/W, respectively) attain almost all the potential advantages of CW operation. At $\gamma^{(0)} > 0.2$ A/W there are no cost reductions since we assume a minimum of 75 MW of auxiliary power is still needed (for ignition). Above $\gamma^{(0)} \approx 1.0$ A/W we see increases in P_{net} become negligible.

Lastly, we are reminded that the CW cycle has $N_f \approx 200$, so fatigue is not a factor. This facet of the CW operating mode may give it a crucial advantage over the pulsed modes in the effort to attain high reactor availability.

5.3 Internal Transformer (IT) Cycle

Even if it is not possible to achieve $\gamma^{(0)} \gtrsim 0.07$ it may still be possible to reduce reactor costs below those for the OH cycle if the IT operating mode is employed since the IT cycle dispenses with the OHC and its dump resistor/switch. In addition, maintaining the toroidal current nearly constant may reduce the likelihood of disruptions, although this is not guaranteed since density, temperature, and beta fluctuations do occur, and more frequently than for the OH cycle.

The capital cost and power balance depend on the overdrive ratio, θ, and the ratio of current drive efficiency to electron density during the overdrive phase, γ/n_{20}'. Additionally, the driver power is minimized by enhancing plasma resistance during overdrive, and we find the most likely case has $L/R' = 171$ s. (In comparison, $L/R = 5590$ s during the burn if $R = R_{SP}$.) Finally, the dwell and EFC ramp times are optimized to minimize the total ETS and driver cost. The results for the total capital cost are given in Fig. 23 for the 8-m reactor with water thermal storge and near-term magnet costs (C_I). The current drive system is costed at \$1.5/W, and the magnet fatigue is based on reasonably long t_f, assuming $R = R_{SP}$ during the burn. We have every confidence that noninductive current drive can achieve γ/n_{20}' in the range displayed. For example, PLT has documented $\gamma = 0.014$ A/W (scaled from its $R_0 = 1.32$ m to an 8-m reactor) with lower hybrid drive at $n_{20}' = 0.03$ to attain $\gamma/n_{20}' = 0.47$. We note from the figure that there are only small benefits from increasing γ/n_{20}' beyond unity.

At small θ (≈ 1.2) this cycle offers large cost savings, with the cost ≈ 1.25 times STARFIRE, compared to the OH cycle which, for $R = R_{SP}$ and near-term technology, costs ≈ 1.38 times STARFIRE. At such small θ the current drive system is relatively small so the cost is insensitive to this cost account. The cost savings result from the reduced ETS compared to that for the conventional cycle (see Fig. 20). However, at $\theta \approx 1.2$ the critical drawback for the IT cycle is the large increase in N_f compared to the OH cycle. For example, with $t_f \approx 600$ s disruptions must be much less frequent

($f \lesssim 10^{-4}$) or less damaging than for the OH cycle (which has $t_f \approx 6000$ s) in order to withstand thermal damage to the first wall and limiter. Operation at higher θ still results in a larger number of fusion cycles than the OH operating mode and is also less credible due to the larger $\Delta I/I_0$ resulting from the stronger overdrive. Indeed, all the cost figures are suspect in this figure since fatigue is so severe for the TFC structure (cf. Fig. 14), i.e., it is not clear that TF coils can be fabricated in the fashion utilized by STARFIRE.

The situation deteriorates if the resistance should be anomalously large. For example, with $R = 2.5\ R_{SP}$, N_f probably exceeds 1.0×10^6. This results in a more expensive capital cost (due to increased structure to withstand mechanical fatigue) and probably a lower availability (due to more frequent failures related to thermal cycles). In addition, the duty factor and net power suffer significantly for increasing values of R, in contrast to the OH cycle.

5.4 Hybrid Cycle

This cycle appears more attractive than either the OH or IT cycles for relatively low values of γ. We consider both $\gamma/\hat{n}_{20}$ and the OHC flux (or, equivalently, the OHC field, B_{OH}) as variables. We set the current drive system cost to be \$1.5/W, but we find the total cost is insensitive to the exact driver cost for $\gamma/\hat{n}_{20} \gtrsim 1.0$ or for $B_{OH} \lesssim 2$ T. As discussed in Sec. 4, the dwell and EFC ramp periods as well as the requisite current drive power are determined by minimizing the ETS and current drive system cost.

Figure 24 shows the total cost with water thermal storage and near-term magnet costs. It also takes the pessimistic assumption of high plasma resistance, $R = 2.5\ R_{SP}$, which results in relatively short burns and a large number of fatigue cycles. We find, for the same burn length as attainable with the OH cycle under these circumstances ($t_f \approx 3100$ s), the hybrid cycle is cheaper than the OH cycle whenever $\gamma/\hat{n}_{20} \gtrsim 0.3$. This is because the OHC is smaller and because the dump resistor/switch is absent. Since the toroidal current is held nearly constant in this operating mode the frequency of disruptions might possibly be somewhat lower than for the conventional OH burn cycle. If we could permit, say, twice as many burn cycles ($N_f \sim 6 \times 10^5$) with short $t_f \approx 1600$ s, then we find even greater cost savings. For typical $\gamma/\hat{n}_{20}$ we find the minimum total cost ≈1.25 times the STARFIRE cost, whereas the comparable (water storage, near-term magnets) reactor operating under the OH cycle cost

≈1.43 times the STARFIRE cost. On the other hand, if thermal cycling is a particularly severe limitation to limiter or first wall life we could opt for slightly longer burns than the OH cycle allows. At B_{OH} = 10 T the hybrid cycle achieves $t_f \approx 4800$ s compared to $t_f \approx 3100$ for the OH cycle, and if $\gamma/n_{20}' \gtrsim 0.5$ the hybrid case still results in a less expensive reactor. Another significant conclusion follows from a comparison of Figs. 23 and 24, viz., for any given burn length t_f in excess of ~1500 s the hybrid cycle is always cheaper than the IT burn cycle. This stems from the very high ETS cost (see Fig. 20) incurred at large overdrive ratio θ.

The same conclusions are reached for the hybrid cycle with lithium/sodium thermal storage and long-term magnet cost projections (C_{II}). These assumptions and a more optimistic plasma resistance, $R = R_{SP}$, are embodied in the results in Fig. 25. Comparison with the appropriate ("Li") curve of Fig. 21 shows the hybrid cycle is always less expensive than the OH cycle provided $\gamma/n_{20}' \gtrsim 0.3$-0.5. For B_{OH} = 10 T the hybrid cycle permits longer burns, $t_f \approx$ 12,000 s, compared to the OH cycle, with $t_f \approx 8000$ s. For shorter burns ($t_f \approx 5000$ s) the hybrid cycle promises costs as low as ~1.13 times STARFIRE, whereas the OH cycle appears to cost ~1.25 times STARFIRE. We can summarize these conclusions: the hybrid cycle is more attractive than the OH cycle provided $\gamma/n_{20}' \gtrsim 0.3$ or, for $n_{20}' = 0.02$, for $\gamma \gtrsim 0.006$. However, the CW cycle is by far the cheapest and best, with an essentially negligible number of fatigue cycles, provided $\gamma \gtrsim 0.07$.

5.5 Synopsis

Our conclusions fall into several categories. In the area of operating goals and material properties we find:

- Double-swing OH operation results in cost savings compared to single swing OH operation.
- For either OH burn cycle we find reactor cost minimizes at fairly long burn times, $t_f \gtrsim$ 10-20 h.
- For any cycle with a fusion period as short as ~1 h there is a first wall and limiter life limit imposed by thermal fatigue, especially if there are frequent or severe disruptions. Thermal fatigue ceases to be a major concern if disruptions are very rare ($f \lesssim 10^{-4}$) or of low

energy density (<200 J/cm^2), if vapor shielding is significant, or if the melt layer is not lost from the affected surface. On the other hand, a single disruption could be fatal if it initiates cracks in the first wall which lead to premature thermal fatigue failure.

- Use of materials with superior thermal fatigue resistance may permit shorter fusion burns for a given replacement period of the reactor component. However, if structural materials such as vanadium are selected for their high radiation resistance, then there appears to be a need to extend burn lengths in order that thermal fatigue not prevent the achievement of longer in-reactor life. Considering the uncertainties surrounding disruption-induced damage, the full benefits of radiation resistant materials can probably only be guaranteed with the CW burn cycle.

Regarding issues of plasma physics we can reach several conclusions:

- If very low plasma edge temperatures (<50 eV) are possible then tungsten could serve as an ideal thin limiter leading edge coating with the result that disruptions and thermal fatigue would have negligible impact on the leading edge lifetime.
- Our understanding of what initiates disruptions must improve. If disruptions are eliminated by merely holding the toroidal current constant, then the IT and hybrid cycles can be attractive compared to the OH cycle. However, if density variations can also trigger disruptions then the CW cycle may be the only good alternative.
- Lower current (higher beta) equilibria are beneficial to tokamak reactors, allowing longer burns for inductive current drive, due to the lower loop voltage, and permitting smaller driver power for non-inductive current drive.
- We can achieve longer inductive burn periods if means are found to substantially lower plasma resistivity, e.g, by lowering Z_{eff}, eliminating trapped electrons, or modifying the electron distribution function.
- On the other hand, the conventional OH cycle appears virtually obsolete since, even for present-day experimental results ($\gamma/n\hat{z}_0 \approx 0.5$), we find noninductive current drive efficiency is adequate to make the

hybrid cycle result in a cheaper reactor. Likewise, for reasonable t_f ($\gtrsim$20 min) the hybrid cycle is better than the IT cycle.

- If noninductive current drive can achieve $\gamma \gtrsim 0.07$ A/W then CW operation is by far the best choice. We should aggressively seek improvements or alternatives (fast wave, low frequency compressional Alfven wave [9]) to the lower hybrid wave for noninductive current drive.

In the area of driver technology we conclude:

- Reductions in driver system cost (to $\lesssim$\$1/W) are always desirable, and we note that lower frequency (~1-100 MHz) drivers come closest to this goal. However, the OH reactor cycle costs ~20-25% more than STARFIRE, so we infer that an equivalent sum (~\$400-500 M) can be spent on a current driver system before the CW reactor would become more expensive than the OH reactor.

- Of greater significance than cost is the overall power efficiency of the current drive system. Drivers projected to have low η_d (e.g. ECRH) need higher γ to achieve acceptable net reactor power with CW operation.

It is difficult to make sweeping judgments of the relative merits of tokamak burn cycles because a power reactor is such a complex machine with so many operating variables. Yet, in addition to the general trends we have explored, we can point to two other aspects of this problem which are hard to quantify but may be pivotal to the commercial success of tokamaks. First, noninductive current generation may provide an opportunity to tailor the current density profile in order to achieve very stable equalibria. This extra flexibility may not be so easily achieved inductively, and thus CW operation may permit operation at higher β than the OH burn cycle. Finally, the very complexity of a tokamak reactor is a tremendous incentive to achieve CW operation. At this early stage we cannot possibly estimate the reliabilty of millions of components, pumps, valves, motors, etc., when operating through repeated transients. Reliability and, hence, availability is doubtless far easier to achieve with CW operation, and this will weigh heavily in the final choice among burn cycles.

ACKNOWLEDGMENTS

We wish to thank D. Metzler for providing the curves in Fig. 16. Both D. L. Smith and R. F. Mattas contributed significantly to our understanding of fusion materials problems.

REFERENCES

[1] C. C. Baker et al., Nucl. Engrg. Des. 63 (1981) 199; for complete report see C. C. Baker et al., "STARFIRE - A Commercial Tokamak Fusion Power Plant Study", Argonne National Laboratory Report, ANL/FPP/80-1 (1980).

[2] N. J. Fisch, "Operating Tokamaks with Steady-State Toroidal Current," Princeton Plasma Physics Laboratory Report, PPPL-1772 (1981).

[3] N. J. Fisch, in Proc. 3rd Joint Varenna-Grenoble Intern. Symp. on Heating in Toroidal Plasmas, EUR7979EN, Vol. III (1982) 841.

[4] C E. Singer and D. R. Mikkelsen, J. Fusion Energy 3 (1983) 13.

[5] R. A. Bolton et al., in Proc. 3rd Top. Mtg. on Technology of Controlled Nuclear Fusion, CONF-780508, Vol. II (1978) 824.

[6] D. A. East et al., "Tokamak Burn Cycle Study: A Data Base for Comparing Long Pulse and Steady-State Power Reactors," Argonne National Laboratory Report, ANL/FPP/TM-178 (1983).

[7] D. A. East et al., J. Fus. Energy 2 (1982) 83.

[8] N. J. Fisch, Phys. Rev. Lett. 41 (1978) 873.

[9] N. J. Fisch and C. F. F. Karney, Phys. Fluids 24 (1981) 27.

[10] N. J. Fisch and A. H. Boozer, Phys. Rev. Lett. 45 (1980) 720.

[11] M. Porkolab et al., "Lower Hybrid Current Drive and Heating Experiments at the 1-MW RF Power Level on Alcator C," presented at 11th European Conf. on Controlled Fusion and Plasma Physics, Aachen, West Germany, September 1983.

[12] R. Motley et al., "Noninductive Current Drive in Tokamaks," in Proc. of IAEA Technical Committee Meeting, Culham, England, CLM-CD (1983), Vol. II (1983) 299.

[13] N. J. Fisch, Nucl. Fusion 21 (1981) 15.

[14] T. Ohkawa, Nucl. Fusion 10 (1970) 185.

[15] R. L. Reid et al., "Large Aspect Ratio Study," in Proc. 8th Symp. on Engineering Problems of Fusion Research, Vol. I (1979) 427.

[16] J. N. Brooks and R. L. Kustom, "Power Supply Requirements for a Tokamak Fusion Reactor," Argonne National Laboratory Report, ANL/FPP/TM-119 (1979).

[17] L. Bromberg, D. R. Cohn, and J. E. C. Williams, J. Fusion Energy 3 (1983) 63.

[18] D. R. Mikkelsen and C. E. Singer, Nucl. Technol./Fusion 4 (1983) 237.

[19] U.S. Contribution to the International Tokamak Reactor Phase 2A Workshop, USA FED-INTOR/82-1 (1982), Georgia Institute of Technology, Atlanta.

[20] D. L. Smith et al, "Fusion Reactor Blanket/Shield Design Study," Argonne National Laboratory Report, ANL/FPP/79-1 (1979) Chap. 7.

[21] R. F. Mattas and D. L. Smith, Nucl. Technol. **39** (1978) 186.

[22] R. F. Mattas, Fusion Component Lifetime Analysis, Argonne National Laboratory Report, ANL/FPP/TM-160 (1982).

[23] A. M. Hassanein, G. L. Kulcinski, and W. G. Wolfer, J. Nucl. Mater. **103/104** (1981) 321.

[24] C. A. Flanagan et al., "Fusion Engineering Device Design Description," Oak Ridge National Laboratory Report, ORNL/TM-7948/V1 (1981).

[25] K. Evans, Jr., D. A. Ehst, and P. Messerschmidt, in Proc. 3rd Top. Mtg. on Technology of Controlled Nuclear Fusion, CONF-780508, Vol. II (1978) 1084.

[26] L. Turner and M. Abdou, "Computational Model for Superconducting Toroidal-field Magnets for a Tokamak Reactor," Argonne National Laboratory Report, ANL/FPP/TM-88 (1977).

[27] R. J. Hooper and B. L. Hunter, "Structural Design Procedures for FED," in Proc. 9th Symp. on Engineering Problems of Fusion Research, IEEE Pub. No. 81CH1715-2-NPS, Vol. I (1981) 539.

[28] S. S. Kalsi and R. J. Hooper, "Calculation of Eddy Current Loses in Toroidal Field Coil Casing," **ibid.**, Vol. 1 (1981) 131.

[29] G. A. Deis, "Thermal Cycling Effects in Tokamak Blanket Components," **ibid.**, Vol. II (1981) 1783.

[30] C. H. Buchanan, "Energy Storage for Tokamak Reactor Cycles," Princeton Plasma Physics Laboratory Report, PPPL-1511 (1979).

[31] R. J. Temkin et al., "Design Study of a Tokamak Power Reactor with an Electron Cyclotron Resonance Heating System," MIT Plasma Fusion Center Report, PFC/RR-79-20 (1979).

[32] B. W. Reed et al., "Preliminary Report on the Development of rf Auxiliary Heating Systems for TEPR-1," Princeton Plasma Physics Laboratory Report, PPPL-1410 (1977).

[33] J. N. Brooks and R. L. Kustom, Nucl. Technol. **46** (1979) 61.

[34] F. Petree and R. L. Cassel, "Ohmic Heating System for the TFTR Tokamak," in Proc. 7th Symp. on Engineering Problems of Fusion Research, IEEE Pub. No. 77CH1267-4 NPS, Vol. I (1977) 891.

Distribution for ANL/FPP/TM-185

Internal:

C. Baker
M. Billone
C. Boley
J. Brooks
Y. Cha
R. Clemmer
D. Ehst (10)
K. Evans
P. Finn
Y. Gohar
D. Gruen
A. Hassanein
C. Johnson
J. Jung
S. Kim
L. LeSage
R. Leonard
B. Loomis
S. Majumdar
R. Mattas
B. Misra
R. Nygren
B. Picologlou
J. Roberts
D. Smith
H. Stevens
D.-K. Sze
L. Turner
S.-T. Yang
ANL Patent Dept.
FP Program (10)
ANL Contract File
ANL Libraries (2)
TIS Files (6)

External:

DOE-TIC, for distribution per UC-20,20a,20b,20c,20d (237)
Manager, Chicago Operations Office, DOE
University of Chicago Special Committee for the Fusion Program:
S. Baron, Burns & Roe, Inc.
H. Forsen, Bechtel Group, Inc.
J. Maniscalco, TRW, Inc.
G. Miley, University of Illinois-Urbana
P. Reardon, Brookhaven National Laboratory
P. Rutherford, Princeton Plasma Physics Laboratory
D. Steiner, Rensselaer Polytechnic Institute
K. Symon, University of Wisconsin-Madison
K. Thomassen, Lawrence Livermore National Laboratory
A. Bers, Massachusetts Institute of Technology
D. Berwald, TRW
L. Bromberg, Massachusetts Institute of Technology
E. Canobbio, Max-Planck Institute fur Plasmaphysik, West Germany
D. Cohn, Massachusetts Institute of Technology
P. Colestock, Princeton Plasma Physics Laboratory
R. Conn, University of California-Los Angeles
N. Fisch, Princeton Plasma Physics Laboratory
R. Hancox, Culham Laboratory, UKAEA, England
R. Harvey, GA Technologies Inc.
A. B. B. Kadomtsev, I. V. Kurchatov Institute of Atomic Energy, U.S.S.R.
R. Klima, Czechoslovak Academy of Sciences, Czechoslovakia
R. Krakowski, Los Alamos National Laboratory
G. Kulcinski, University of Wisconsin, Madison
J. Lister, Centre de Recherches en Physique des Plasma, Switzerland
D. Metzler, FEDC, Oak Ridge National Laboratory
J. Meyer, Massachusetts Institute of Technology
D. Mikkelsen, Princeton Plasma Physics Laboratory
Y.-K. Peng, FEDC, Oak Ridge National Laboratory
D. Ross, University of Texas-Austin
J. Schmidt, Princeton Plasma Physics Laboratory
J. Schultz, Massachusetts Institute of Technology

T. Shannon, FEDC, Oak Ridge National Laboratory
J. Sheffield, Oak Ridge National Laboratory
C. Singer, Princeton Plasma Physics Laboratory
W. M. Stacey, Jr., Georgia Institute of Technology
D. Start, Culham Laboratory, UKEA, Abingdon, England
W. Stodiek, Princeton Plasma Physics Laboratory
T. Yamamoto, Japan Atomic Energy Research Institute
Library, Centre de Etudes Nucleaires de Fontenay, France
Library, Centre de Etudes Nucleaires de Grenoble, France
Library, Centre de Etudes Nucleaires de Saclay, France
Library, Centre de Recherches en Physique des Plasma, Lausanne, Switzerland
Library, FOM-Institute voor Plasma-Fysika, Jutphass, Netherlands
Library, Comitato Nazionale per l'Energia Nucleare, Rome, Italy
Library, Joint Research Centre, Ispra, Italy
Library, Japan Atomic Energy Research Institute, Ibaraki, Japan
Library, Max Planck Institute fur Plasmaphytsik, Garching, Germany
Library, Culham Laboratory, UKAEA, Abingdon, England
Library, Laboratorio Gas Ionizati, Frascatti, Italy

LIST OF FIGURES (Contd.)

LIST OF TABLES